The organization of scalar mixing by coherent structures

An experimental study

J.Reijtenbagh

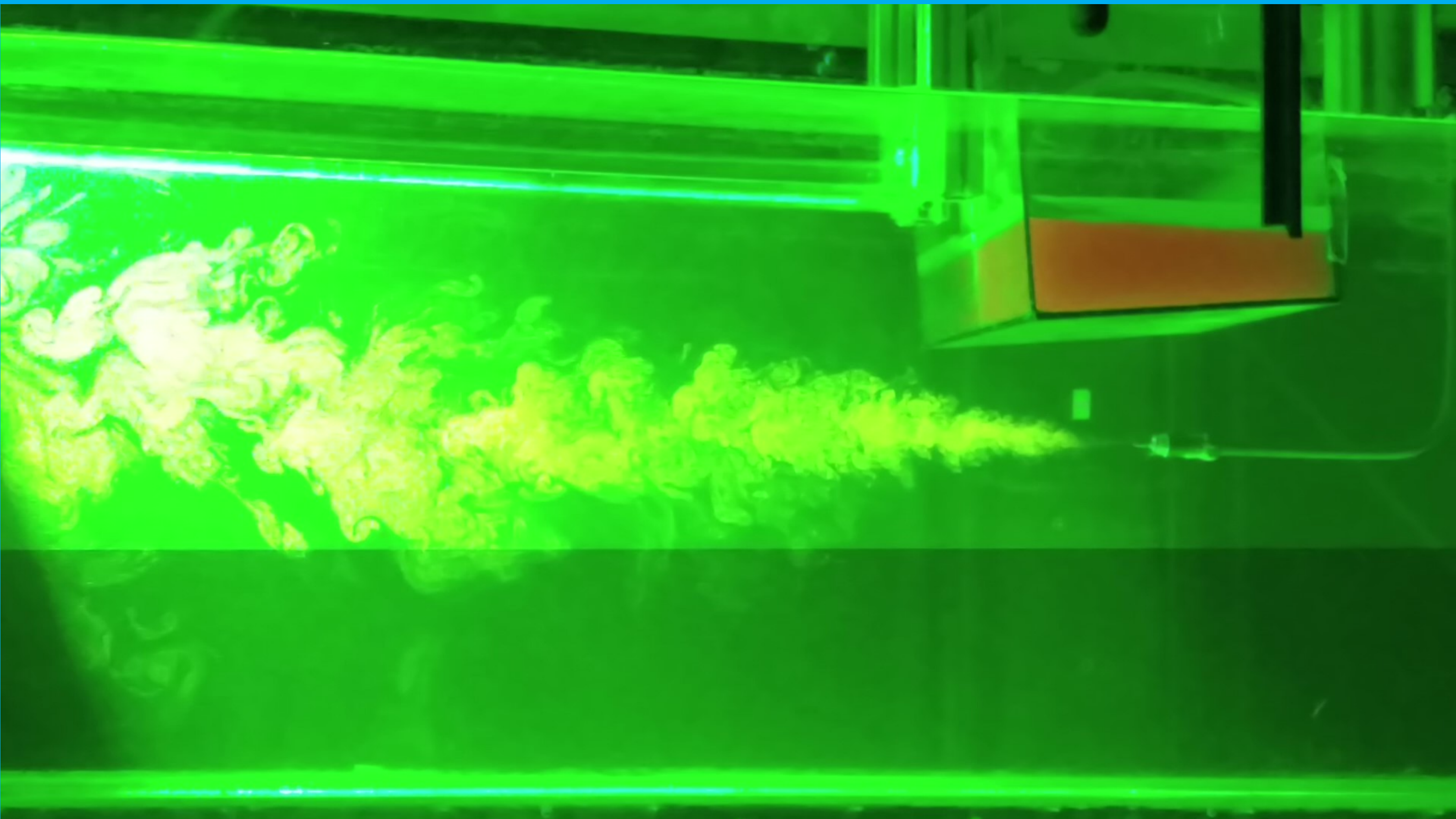

TUDelft

The organization of scalar mixing by coherent structures

An experimental study

by

J.Reijtenbagh

to obtain the degree of Master of Science
at the Delft University of Technology,
to be defended publicly on Monday November 30, 2020 at 10:00 AM.

Student number:	4246179	
Project duration:	September 30, 2019 – November 26, 2020	
Thesis committee:	Prof. dr. ir. W. van de Water,	TU Delft, supervisor
	Prof. dr. ir. J. Westerweel,	TU Delft, supervisor
	Dr.Ir. R. Pecnik,	TU Delft

TUDelft

Acknowledgements

First and foremost, I would like thank prof. dr. ir. Willem van de Water for his daily supervision during this project. I am very grateful for his great enthusiasm and involvement in the project, which convinced me to choose this project en helped me when get over some difficulties that occurred during the project. Although it was not always easy to speak regularly, we still managed to have online meetings often, for which I would also like to thank him, because the many fruitful discussions we had on several topics in this thesis gave me a lot of new insights. Hopefully this was mutual. Finally I would like to thank him for the extensive feedback he gave me during the experimental phase of this project, and even more during the writing of this thesis.

I would also like to thank prof. dr. ir. Jerry Westerweel for his supervision. Although we did not meet regularly, our discussions were always very helpful and your feedback helped me a lot. Especially in the final stages of this project you helped me making progress and I am looking forward to continue working with you when this project is finished.

At the end of the experiments the setup was quite impressive, with a lot of different components. This final setup could not have been completed without the help of Edwin, Gertjan, Jan and Jasper. Their great technical know-how on several aspects of the setup made my part of doing the experiments much easier and for that I am very grateful. With their help I was able to keep the overview of the project and even when I could only come to the lab one or two days per week, they always found the time to help me with my problems regarding the setup and every time I needed something you all were very quick with solutions or fabrications that solved my problems. So again: thank you very much for that.

Furthermore I would like to thank everyone else I met in the department and during my master with whom I had fruitful discussions on doing experiments and solving other problems, with special thanks to Bram, Jeroen and Koen, with whom I spent most of my time during this project working alongside each other. Your tips on all kinds of things helped me a lot, as well as the times we spent when we all needed a short break.

Finally I would like to thanks my family and friends for their support during this whole project.

J.Reijtenbagh
Delft, November 2020

Abstract

Turbulent scalar mixing is prominent in all sorts of situations, being it in air pollution or making tea. However, this does not often lead to a homogeneously mixed fluid, but rather leads to regions of higher concentrations next to regions with significantly lower concentrations. This can be characterized by dividing the concentration field in a turbulent flow into a few regions that have almost the same concentration: Uniform Concentration Zones. How these Uniform Concentration Zones are organized is yet unclear, but a possible candidate in the velocity field is the use of Lagrangian Coherent Structures. These structures are, in principle, transfer barriers in the flow and defined as local maxima of the Finite Time Lyapunov Exponent (FTLE), which is a measure of exponential fluid-separation over time. In order to successfully apply the concept of Lagrangian Coherent Structures in an experiment, turbulent structures should remain in focus long enough to measure the exponential separation of fluid parcels. As almost all fully developed turbulence comes with a mean flow, the observation time in an Eulerian field-of-view is too short. Therefore an experiment was designed to move the observation equipment with the mean flow. With this experimental setup, the concentration field and the velocity field are measured simultaneously via respectively LIF and PIV. Comparing the Uniform Concentration Zones with both the forward and backward time FTLE-field, shows that there is not much correlation between the concentration field and the forward time FTLE. However, local maxima of the backward time FTLE seem to overlap often with boundaries between Uniform Concentration Zones.

Nomenclature

Acronyms

FCM	Fuzzy Cluster Method
FTLE	Finite Time Lyapunov Exponent
KDE	Kernel Density Estimation
LCS	Lagrangian Coherent Structure
LIF	Laser Induced Fluorescence
PDF	Probability Density Function
PIV	Particle Image Velocimetry
PTU	Programmable Timing Unit
UCZ	Uniform Concentration Zones
UMZ	Uniform Momentum Zones

Latin symbols

B_u	Decay parameter	[-]
C	Cauchy-Green strain tensor	[-]
$c*$	Scalar concentration	[g/l]
c_k	Cluster centroid	[-]
D_{mk}	Difference between observation m and cluster centroid k	[-]
$F_{t_0}^{t_1}$	Flow map	[-]
G	Kernel function	[-]
h	Kernel width	[-]
I	Image intensity	[counts]
K	Number of zones	[-]
l	Jet half width	[m]
M_0	Image magnification	[-]
T_i	Integration time	[s]
U_0	Nozzle outlet velocity	[m/s]
U_C	Camera velocity	[m/s]
u_{mk}	Membership coefficient of observation m to cluster k	[-]
U_S	Centerline velocity	[m/s]

Greek symbols

η	Kolmogorov length	$[m]$
λ_{max}	Highest eigenvalue Cauchy Green tensor	[-]
ν	Kinematic viscosity	$[m^2/s]$
σ	Finite Time Lyapunov Exponent	$[1/s]$

Contents

Introduction

Turbulent scalar mixing is prominent in all sorts of situations, being it in air pollution or making tea. However, this does not often lead to a homogeneously mixed fluid, but rather leads to regions of higher concentrations next to regions with significantly lower concentrations. This behaviour can be characterized by dividing this scalar concentration field in a small number of regions that have almost the same scalar concentration. We call these regions Uniform Concentration Zones (UCZs). An example of Uniform Concentration Zones is shown in Figure 1.

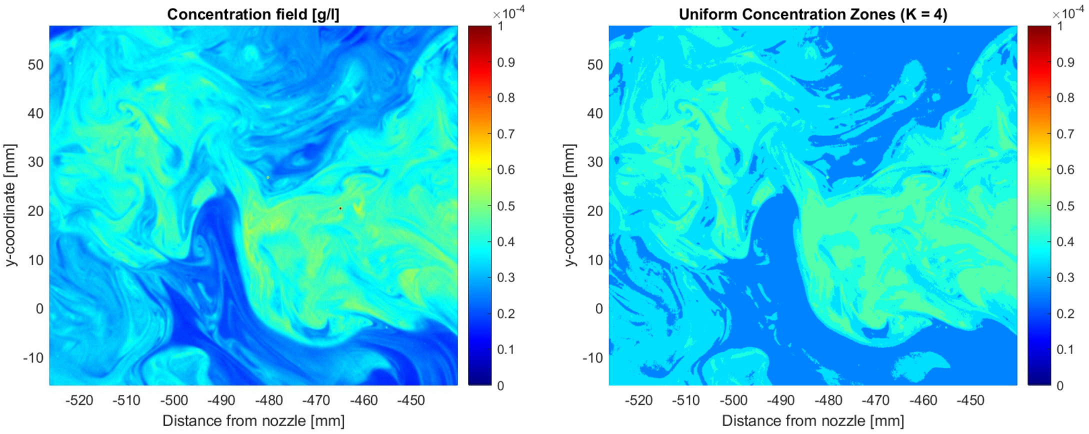

Figure 1: An example of Uniform Concentration Zones. Left: A snapshot of a concentration field. Right: The same concentration field divided into 4 Uniform Concentration Zones.

The left part of Figure 1 shows a raw instantaneous concentration field in a turbulent jet. This field shows patches where the concentration does not vary much, bordered by a sharp concentration gradient from other patches with almost uniform concentration. The idea of UCZs is to unite these regions into a small number of zones, each with a characteristic concentration for the whole zone. An example of this is shown in the right part of Figure 1.

The idea of Uniform Concentration Zones is reminiscent of Uniform Momentum Zones (UMZs), as introduced by Meinhart and Adrian [15]. Their research into a turbulent boundary layer showed, by subtracting a constant velocity from the streamwise velocity component in snapshots of the flow field, large regions with almost uniform momentum in snapshots of the velocity field. When making a Probability Density Function (PDF) of the velocities of these snapshots, these zones correspond with distinct peaks in the PDF. Eisma [7] showed that the boundaries of UMZs are often formed by thin layers that contain high shear.

Previous research by Eisma [6] showed that the organization of these Uniform Concentration Zones somewhat overlapped with Uniform Momentum Zones. Therefore the boundaries of UCZs also somewhat overlap with layers of high shear. Shear layers show a high gradient in velocity and are therefore logical boundaries for Uniform Momentum Zones, but not necessarily for Uniform Concentration Zones. For this reason we will look for structures in the velocity field that are more suited to coincide with concentration gradients compared to velocity gradients. A characteristic of the velocity field that might be a better candidate to organize the boundaries of UCZs is the Lagrangian Coherent Structure (LCS), which are in principle lines in a 2-dimensional flow field that act as transfer barriers in a turbulent flow [11, 20]. The most common and robust way to find LCSs is to look at the Finite Time Lyapunov Exponent (FTLE), and more specifically, ridges in this FTLE-field.

The similarity between the distribution of a passive scalar, such as a dye, and structures in a turbulent velocity field has been investigated previously. Swanson and Ottino [22] looked at the dispersion of a dye inside flow of a bearing, and showed similarities between the chaotic dispersion of droplets of a dye and the Poincaré map, which can be seen as a predecessor of the FTLE-field. Pentek et al. [18] observed the pattern of tracing dye in a vortex pair and observed a similar pattern in the unstable manifolds of the velocity field, which, according to Haller [11], align closely to contours of the FTLE-field. Other research, like the one from Brunton and Rowley [5], shows how tracer particles move from repelling LCSs to attracting LCSs.

Voth et al. [24] looked at the similarity between the concentration field and the past stretching field, which is similar to an FTLE-field. This was done in a controlled periodic flow, with only weak turbulence and showed the correspondence between stretching fields and the Poincaré map of the flow. Twardos et al. [23] also linked the concentration field to stretching field and looked at the FTLE in the same flow, but also for a low Reynolds number, so with weak turbulence. Other experiments at higher Reynolds numbers such as those performed by Mathur et al. [14] looked more into LCSs and the corresponding FTLE-field, but still in a restricted, nearly two-dimensional flow.

In order to successfully apply the concept of LCSs in an experiment, turbulent structures should remain in focus long enough to measure the exponential separation of fluid parcels. As almost all fully developed turbulence comes with a mean flow, the observation time in an Eulerian field-of-view is too short. Therefore an experiment was designed to move the observation equipment with the mean flow.

This thesis describes experiments done in the Aero- and Hydrodynamics Lab at the 3ME-faculty of the TU Delft. The experiments consist of simultaneous Particle Image Velomecitry (PIV)- and Laser Induced Fluorescence (LIF)-measurements, to measure respectively the velocity and scalar concentration fields of a turbulent jet inside a water tunnel. These measurements are done with cameras that move along with the flow while filming, so the same fluid remains longer in the field-of-view of the cameras, which makes these measurements more suitable for finding LCSs than the data of Eisma [6, 7]. Furthermore, this thesis describes the methods to find UCZs and the FTLE-field and gives some preliminary results of UCZs and the FTLE-field in the flow and the correlation between the two, to find an answer to the question: How do ridges in the FTLE-field of a flow correlate with the boundaries of Uniform Concentration Zones?

Outline

First, a more extensive explanation of UCZs and LCSs can be find in Chapter 1. In Chapter 2 the algorithms to find UCZs and LCSs are discussed. Chapter 3 describes the parameter study needed to design the experiment. The experimental setup and measurement procedures are shown in Chapter 4, and preparatory measurements, such as turbulent statistics and calibration of the concentration measurements, and their results are described in Chapter 5. Finally, Chapter 6 discusses the results of the measurements, while Chapter 7 presents a conclusion and gives some recommendations for further investigation.

1

Theoretical concepts

This chapter describes the two fundamental concepts mentioned in the introduction: Lagrangian Coherent Structures and Uniform Concentration Zones. First, the way LCSs are defined and how they are found are described, as well as an illustrative example. Then UCZs are explained as well as methods to find these zones.

1.1. Lagrangian Coherent Structures

1.1.1. Definitions

Lagrangian Coherent Structures (LCSs) are invariant material lines in a turbulent flow that, as the name suggests, move along with the flow and are obtained from fluid trajectories. The main trait of an LCS is the fact that, when an LCS is well defined, the material flux across an LCS is negligible, as demonstrated by Shadden [20]. This means that a well defined LCS acts as a transfer barrier for an added scalar that is advected with the flow.

Coherent Structures play a significant role in transport in laminar, and even more so in turbulent flows. However, determining these structures in an objective way is a difficult task. Most Eulerian structures are not suitable due to a lack of an accepted definition and the inability to capture flow properties in unsteady flow. Therefore LCSs may give a better view on fluid mixing, because they are more stable and more straightforward to determine in unsteady turbulent flows [14].

There are two fundamental types of LCSs: Repelling and attracting LCSs. According to Mathur et al. [14] repelling LCSs are found by looking at the future of the velocity field, and correspond with the stable manifolds for trajectories in the flow. Attracting LCSs are found by looking at the past velocity field and correspond with the unstable manifolds for trajectories. This is emphasized by Wilson et al. [27], who showed how the intersection of a repelling and an attracting LCS behaved like a saddle point in the flow, with a repelling and attracting LCS acting as the respectively stable and unstable manifolds of this hyperbolic core.

There are many methods to find coherent structures in flows, each with its strengths and weaknesses. Hadjighasem et al. [10] described some of these methods and compared them in different flow fields, both numerical and experimental. One of the most classical and robust methods of determining LCSs is finding ridges in the Finite Time Lyapunov Exponent (FTLE) field. This objective method looks at the exponential growth of the separation between two fluid parcels that start close together.

1.1.2. The Finite Time Lyapunov Exponent

As mentioned, Hyperbolic LCSs are mostly found on the ridges of the Finite Time Lyapunov Exponent (FTLE) field [20]. The FTLE is a characteristic of the flow field that describes the exponential separation fluid parcels that start infinitesimally close together. A local maximum of this FTLE-field indicates a high separation of fluid parcels, which describe LCSs. To calculate this FTLE, a flow map is needed as defined in Equation 1.1:

$$F_{t_0}^{t}(\boldsymbol{x_0}) = \boldsymbol{x}(t; t_0, \boldsymbol{x_0}) \tag{1.1}$$

This flow map describes the location $\boldsymbol{x}$ at a certain time t of fluid parcels that started at location $\boldsymbol{x_0}$ at initial time t_0.

If we take the gradient of the flow $\nabla F_{t_0}^{t}(\boldsymbol{x_0})$, we can calculate the Cauchy-Green strain tensor C for each location $\boldsymbol{x_0}$ following Equation 1.2:

$$C(\boldsymbol{x_0}) = [\nabla F_{t_0}^{t}(\boldsymbol{x_0})]^T \nabla F_{t_0}^{t}(\boldsymbol{x_0}) \tag{1.2}$$

The FTLE-field for each location $\boldsymbol{x_0}$ can then be calculated after finding the eigenvalues of this Cauchy-Green strain tensor following Equation 1.3

$$\sigma_{t_0}^{t}(\boldsymbol{x_0}) = \frac{1}{2|t-t_0|}\log(\lambda_{max}(\boldsymbol{x_0})) \tag{1.3}$$

Here, $\sigma_{t_0}^{t}(\boldsymbol{x_0})$ is the value of the FTLE at location $\boldsymbol{x_0}$, calculated from initial time t_0 to time t and λ_{max} is the largest eigenvalue of the Cauchy-Green strain tensor.

The value of $t - t_0$, the so-called observation time or integration time (T_i) does not need to be positive. When positive, the FTLE-field is called the forward time FTLE-field and shows repelling LCSs. When negative, so when $t < t_0$ the FTLE-field is calculated using velocity fields prior to t_0, and the FTLE-field is called the backward time FTLE-field, which shows attracting LCSs. Since the absolute value of $t - t_0$ is used in the formula, the FTLE-field is still always positive.

LCSs are defined as ridges in the FTLE-field. Shadden et al. [20] describe a second derivative ridge as a line through the (FTLE-)field that has the following properties:

(1) At all points on the ridge, the ridge is a local maximum in the field transverse to the ridge and (2) the steepest decline from the ridge is transverse to the ridge. A more clarifying analogy of a ridge is to consider the FTLE-field as the height of a mountainous area, which means that moving along a ridge is similar to walking on a ridge on a mountain path. In other words, when following the ridge (1) stepping left or right means going down and (2), the steepest decline is also exactly to the left and right.

Ridges can be found by searching for points where these statements are true, which works well on a fine FTLE-field. When the field is too coarse, an algorithm like the one from Allshouse et al. [2] could be used to locate these ridges better. This algorithm first searches for a pre-determined number of local maxima in the FTLE-field, which are the starting points of these ridges. Then a small step is done in the direction of the gradient at on of these maxima, and at this point the FTLE is calculated again. On both sides, perpendicular of the used gradient, another point is introduced on which the FTLE is calculated again. A parabola is fitted on the three points (which all lie on the same line) and the maximum of this parabola is the next point on the ridge. This procedure is repeated until a stopping condition is reached, for example when no maximum is found on the parabola.

The FTLE has a major flaw however. This method does not take the separation of fluid due to high shear into account. When there is high shear, fluid parcels could also get separated, which could result in false positives for LCSs from the FTLE-field. Therefore, Farazmand and Haller [9] introduced additional conditions based on the eigenvectors of the Cauchy-Green strain tensor to find LCSs from the FTLE-field. Another solution to this issue is shown by Haller and Beron-Vera [12], who introduced a method based on geodesics of the Cauchy-Green strain tensor. The least stretching lines in this geodesic theory indicate transfer barriers that are closely related to hyperbolic LCSs. Contrary to regular FTLE-fields, this geodesic theory is not (yet) suited for three-dimensional flow fields.

1.1.3. Example: The Double Gyre

An obvious example of an LCS can be found in the so-called Double Gyre [20], which is a simple time-dependent flow with fixed boundaries that describes two vortices in a rectangular frame with a moving midline, so the vortices expand and contract, as is shown in Figure 1.1.

The Double Gyre is described by the following stream function:

$$\Psi(x,y,t) = A\sin(\pi f(x,t))\sin(\pi y) \tag{1.4}$$

with

$$f(x,t) = a(t)x^2 + b(t)x \tag{1.5}$$

$$a(t) = \epsilon\sin(\omega t) \tag{1.6}$$

$$b(t) = 1 - 2\epsilon\sin(\omega t) \tag{1.7}$$

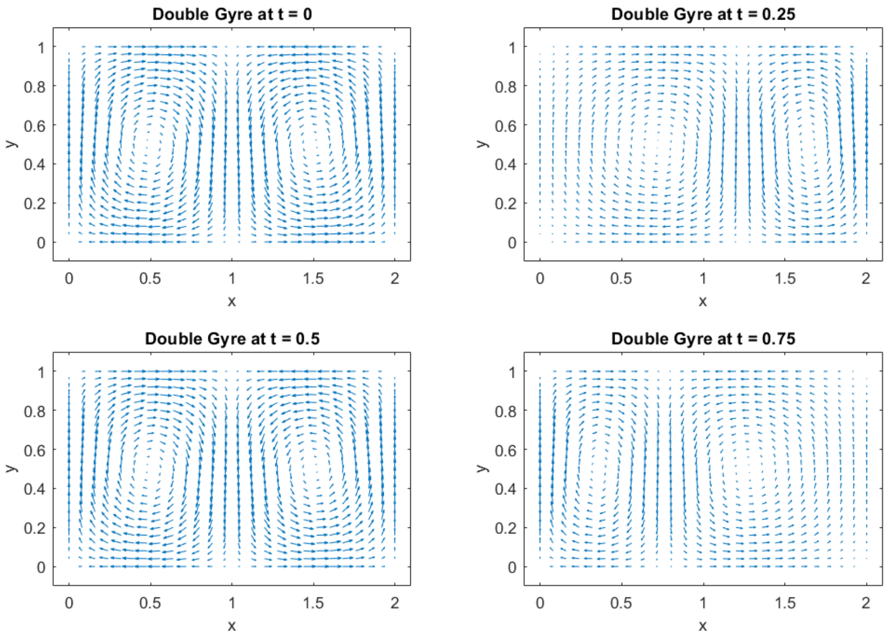

Figure 1.1: The Double Gyre with $A = 0.1$, $\omega = 2\pi$, and $\epsilon = 0.25$ at different timesteps. When $\epsilon = 0$, the flow field is constant as at t = 0

When $\epsilon = 0$, the Double Gyre is stationary and the midline is a separatrix, separating the two vortices and blocking transport from left to right (and vice versa). In the time-dependent case, so when $\epsilon > 0$, this invariant line no longer exists strictly and transport from left to right (and vice versa) is possible in principle. We will demonstrate that also in this case a curve can be identified that controls transport; an LCS.

Figure 1.2 shows the FTLE-field in a Double Gyre in two cases, $\epsilon = 0$ and $\epsilon = 0.25$. The first case shows a clear invariant line in the middle of the domain between the vortices over which there is no transfer. When $\epsilon > 0$, this invariant becomes time-dependent and less obvious, since there is no constant boundary between the vortices in the domain. However, there is still a line that acts like a transfer barrier present in the flow, which is an LCS. The results of Figure 1.2 compare well to the results from Raben et al. [19].

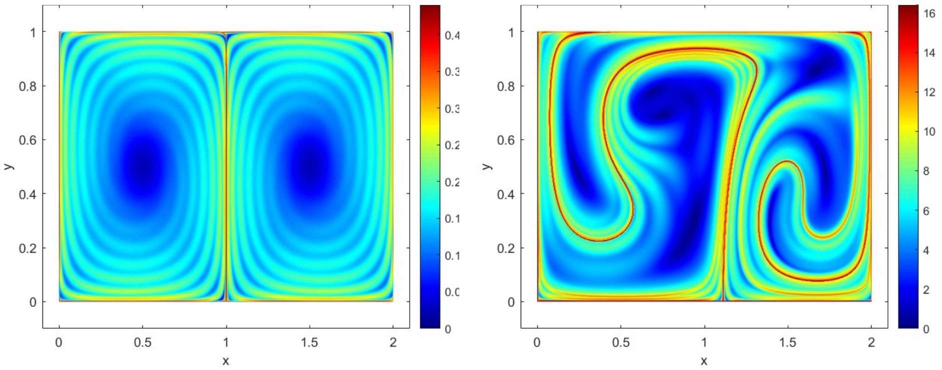

Figure 1.2: FTLE-fields in a Double Gyre at t = 0. The red lines in the FIELD-field are clear ridges and therefore indicate Lagrangian Coherent Structures. Left: Stationary case where $\epsilon = 0$. Right: Non-stationary case where $\epsilon = 0.25$

1.2. Uniform Concentration zones

1.2.1. Definition and example

In his work on turbulent boundary layers, Eisma [6], found by visual inspection that the concentration in a boundary layer is organized in large zones with (almost) uniform concentrations, bordered by sharp gradients. These Uniform Concentration Zones (UCZ) are reminiscent of analogous regions of uniform momentum in turbulent boundary layers, Uniform Momentum Zones (UMZ), which are also investigated by Meinhardt and Adrian. [15]. However, the usual method in finding these zones is arbitrary. The presence of these zones can be seen by visual inspection, but determining the exact boundaries of these zones is usually done by looking at the concentration histogram. In this histogram method, the highest peak in the histogram is found and a Gaussian profile is fitted on this peak. This Gaussian profile is then subtracted from the histogram and a new peak is found, on which a new Gaussian is fitted. This procedure is iterated until there are no significant peaks left. An example of this method on a concentration field is shown in Figure 1.3. Another method in finding UMZs, and therefore UCZs, is given by Fan et al. [8]. This Fuzzy Cluster Method finds different zones in a more statistical manner using c-means clustering. This method is further explained in section 2.1.

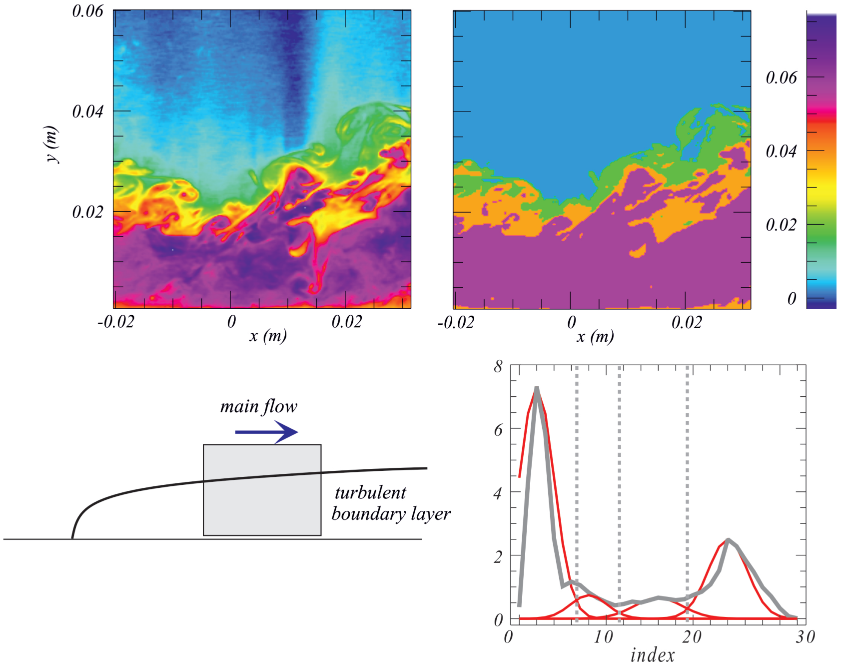

Figure 1.3: An example of Uniform Concentration Zones on the data of Eisma [6, 7]. Top left: Snapshot of a concentration measurement. Top right: The same snapshot divided in 4 UCZs. Bottom left: Schematic of the measurement area. Bottom right: Histogram of the snapshot. The gray line is the histogram, the red lines indicate the 4 Gaussian profiles on the peaks of the histogram and the gray dashed lines indicate the boundaries between UCZs.

1.2.2. Interaction with velocity-field

Eisma [6] showed there is some overlap between the boundaries of UCZs and UMZs. Since the boundaries of UMZs are found at regions with high shear [7], shear lines and the boundaries of UCZs also show some correlation. These are both instantaneous characteristics of the velocity field. One could say the boundaries of UCZs are also instantaneous, but are formed in the past of the flow. Therefore, it makes sense to look for characteristics of the velocity field that say something about the past of the flow field, for instance Lagrangian Coherent Structures and the FTLE-field.

2

Processing Algorithms

This chapter describes the algorithms needed to find the flow characteristics described in the previous chapters. First, a Fuzzy Cluster Method is introduced and explained to find Uniform Concentration Zones. Then two different methods in in determining the FTLE-field are described and lastly the algorithm to calculate the FTLE-field is presented.

2.1. Fuzzy Cluster Method

To find Uniform Concentration Zones a Fuzzy Cluster Method (FCM) is implemented. The method used here is a modified version of the FCM from Fan et al. [8]. Although this method is previously used to find Uniform Momentum Zones instead of Uniform Concentration Zones, the procedure is the same, but with another input. Previous works, such as from Eisma et al. [7] used a histogram method to find UCZs, but such histogram methods rely on user defined thresholds and are therefore not objective. The FCM does not rely on user defined input and should be more robust and easier to automate. This FCM is based on fuzzy c-means clustering, which is a mathematical method of clustering a group of observations or data points. In our case, observations are measured concentrations on each location. Clustering is done by calculating a membership coefficient u_{mk} to each observation m for each different cluster k. This membership coefficient could be seen as the probability that a certain observation belongs in a certain cluster, so when $u_{mk} \approx 1$, the concentration at a certain point m is very close to the characteristic concentration of cluster k. When $u_{mk} \approx 0$, this observation m most probably will not belong to cluster k because its concentration is much closer to another cluster. These characteristic concentrations of each cluster could be determined beforehand, but for this study this will be a weighted average of all concentrations based on the membership coefficient. After all membership coefficients are calculated for each observation with respect to all clusters, the observations then will be assigned the the cluster of which the membership coefficient is the highest. An example of UCZs found by the FCM is shown in Figure 2.1.

2.1.1. The FCM-algorithm

As defined in Chapter 1, UCZs are zones in an instantaneous concentration field, for which the concentration is nearly uniform. This FCM-algorithm assigns each individual pixel to one of the zones $1...K$, where K is the total number of zones. This number of zones is the only user-defined input in this algorithm. Because we want the calculation of UCZs to be as robust as possible, we use the same Kernel Density Estimation (KDE) as used by Fan [8] to determine the number of zones for each separate instantaneous concentration field.

The KDE, adopted from Silverman [21], is a statistical method that estimates the Probability Density Function (PDF) of a set of data. The number of clusters is the number of local maxima of this PDF. This method places a kernel at each observation and a summation of these kernels leads to a smooth PDF describing all concentrations of a instantaneous concentration field. The kernels are given by a kernel function G:

$$\int_{-\infty}^{\infty} G(x)dx = 1 \tag{2.1}$$

This kernel function G could be any function that obeys Equation 2.1. Here, we use a Gaussian distribution for G. The estimated PDF is then given by:

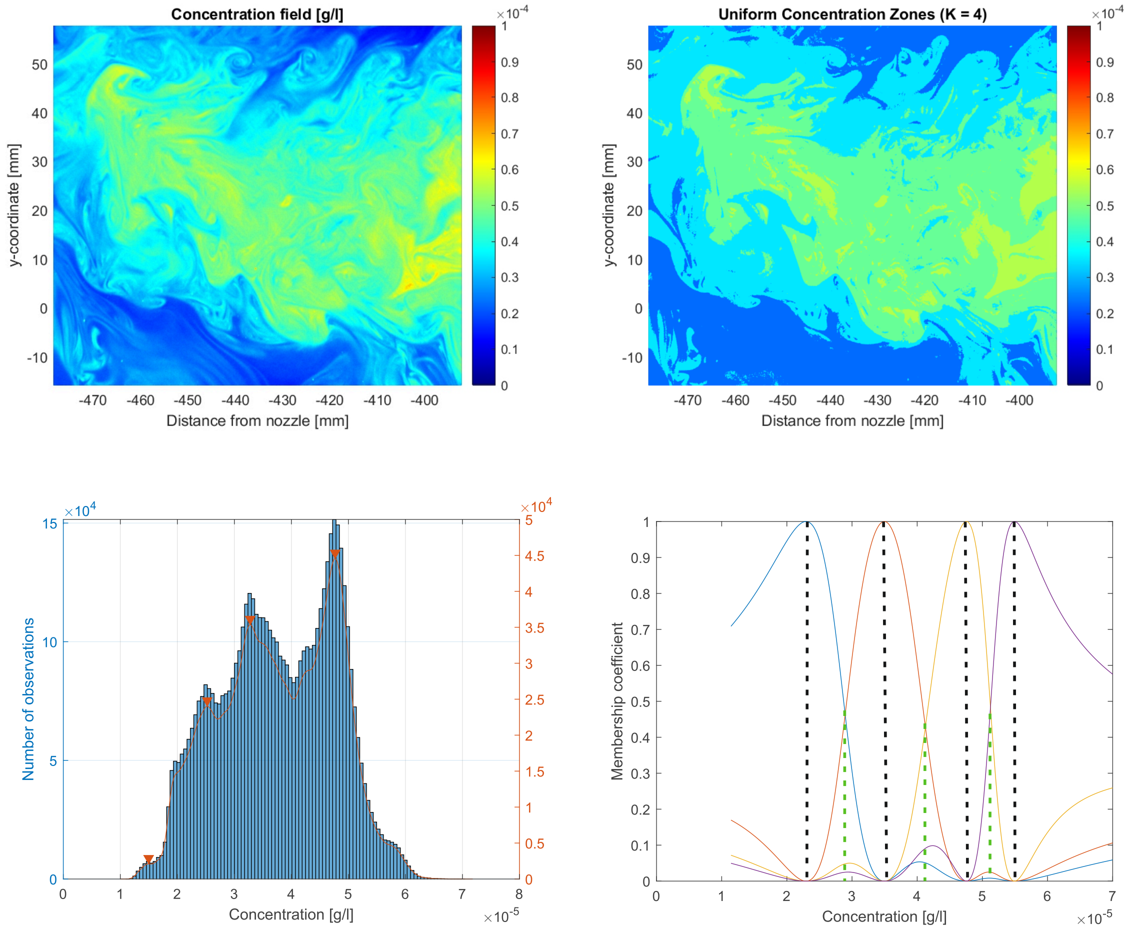

Concentration field [g/l]

Uniform Concentration Zones (K = 4)

Figure 2.1: The Fuzzy Cluster Method applied on the concentration field. Top left: A snapshot of the concentration field. Top right: The same snapshot divided in 4 Uniform Concentration Zones. Bottom left: The PDF of a LIF-Frame estimated with the KDE. The histogram of this frame is in blue, the red line is the estimated PDF. The red arrows indicate peaks in the PDF, in this case there are 4 peaks, so we use K = 4 as input in the Fuzzy Cluster Method. Bottom right: Distribution of membership coefficients U_{mk} across the range of concentrations of one concentration field. The colored lines show the distribution of the membership coefficient u_{mk}, with zone 1 (blue), zone 2 (red), zone 3 (yellow), zone 4 (purple). The black dashed lines show the characteristic concentrations of each zone, where the membership coefficient of that zone is equal to 1. The intersections around $U_{mk} = 0.45$, indicated by the green dashed line, indicate boundaries between UCZs.

$$P(x) = \frac{1}{n}\sum_{i=1}^{n} G\left(\frac{x - X_i}{h}\right) \tag{2.2}$$

Here $P(x)$ is the value of the PDF at concentration x, n is the number of observations, X_i is the concentration of observation i, and h is the width of a kernel. A visual interpretation of equation 2.2 is shown in Figure 2.2. The optimal value of h is given by Fan [8] and is equal to:

$$h = \sigma (4/3)^{0.2} n^{-0.2} \tag{2.3}$$

Here, σ is the standard deviation form all values in the concentration field and n is the number of observations, which is in this case equal to the number of pixels. This expression follows from the requirement that the error in the estimate of a PDF, estimated with Gaussian kernels with width h, is smallest. An example of this kernel density estimation for a certain frame, compared to a histogram is shown in Figure 2.1

Previous investigation into UMZs and UCZs by Eisma [6, 7] uses an extensive histogram method to find UCZs, but the Fuzzy Cluster Method is more robust and has less user-defined inputs. The two important variables in the determination of UCZs via this method are the cluster centroids c_k, which can be seen as the

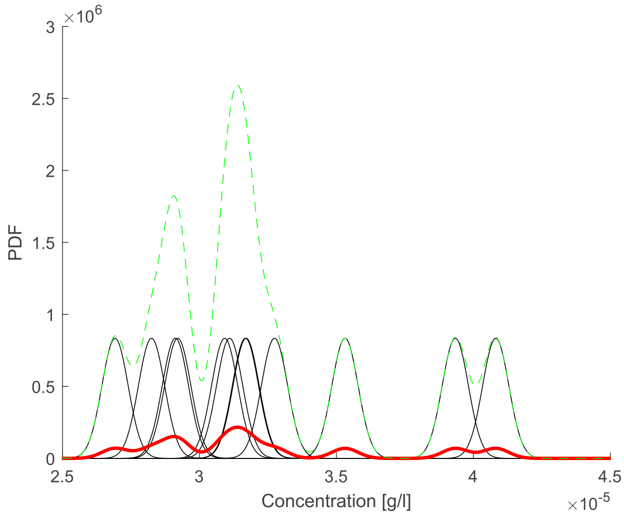

Figure 2.2: Visual representation of the Kernel Density Estimation. The 12 black curves each represent one Gaussian kernel around a certain concentration. These are all summed, which results in the green dashed line. Dividing this green dashed line by 12 results in a curve for which the integral from $-\infty$ to ∞ is equal to one. This is the red line, which indicates the estimated PDF of these 12 observations. The resulting PDF with more observations is shown in Figure 2.1.

characteristic concentration value of each distinct zone, and the membership coefficients u_{mk}, which is the probability that a certain concentration U at observation m belongs in zone k. These variables are calculated by:

$$c_k = \frac{\sum_{m=1}^{N} (u_{mk})^p U_m}{\sum_{m=1}^{N} (u_{mk})^p} \tag{2.4}$$

$$u_{mk} = \left(\sum_{j=1}^{K} (D_{mk}/D_{mj})^{2/(p-1)} \right)^{-1} \tag{2.5}$$

Since u_{mk} is reminiscent of a probability, for each observation m must sum to 1, so:

$$\sum_{k=1}^{K} u_{mk} = 1 \tag{2.6}$$

In Equation 2.5 D_{mk} (D_{mj}) is the distance between observation m and the centroid c_k (c_j) of cluster k (j). The exponent p is the so-called fuzziness parameter. This parameter is usually set to have a value of 2 in practice.

Equations 2.4 and 2.5 are iterated subsequently until all the cluster centroids are converged. This convergence is defined by:

$$|c_k - c_{k0}| < \epsilon \tag{2.7}$$

where c_{k0} and c_k are the centroid k of the previous and current iteration step respectively and ϵ is a convergence parameter.

When the centroids are converged, each observation is assigned to the cluster for which it has the highest membership coefficient u_{mk}. All observations in this cluster are set to the same value, that is the concentration value of the cluster centroid, which results in distinct UCZs. When all observations are assigned to a specific UCZ, we must find the boundaries between the different UCZs. This is done by looking at the concentrations at which one UCZ turns into another UCZ or, in other words, at which concentrations the membership coefficients of two neighbouring clusters intersect, see also Figure 2.1. A contour-plot for these concentrations then gives the boundaries of the UCZs. A more schematic description of this algorithm can be found in Figure 2.6.

2.1.2. Mathematical principles

The equations used to calculate cluster centroids and especially the membership coefficients are not chosen randomly, but have a mathematical meaning. This section shows the proof of how these two main equations of the FCM are found. The equations of the algorithm are adopted from Fan et al. [8], and the proof is adopted from Bezdek [3]. The equation that determines the cluster centroids is defined as a weighted average of all the observations, weighted by the membership coefficient:

$$c_k = \frac{\sum_{m=1}^{N} (u_{mk})^p U_m}{\sum_{m=1}^{N} (u_{mk})^p} \tag{2.8}$$

In which c_k is the centroid of cluster k, the observations are given by $m = 1...N$, u_{mk} is the membership coefficient of observation m to cluster k, U_m is the value of observation m and p is the fuzziness parameter, for which counts: $p > 1$.

The FCM-algorithm is basically a minimization problem, for which the minimization objective is given by the variance of the distances between the observations and the cluster centroids, weighted by the membership coefficients:

$$J_p = \sum_{m=1}^{N} \sum_{k=1}^{K} (u_{mk})^p (D_{mk})^2 \tag{2.9}$$

In which J_p is the variance of the observations with respect to the centroids and D_{mk} is the difference between observation m and cluster centroid c_k. This variance is minimized by a relaxed minimization using Lagrange multipliers α and with Equation 2.6 as a constraint:

$$\Phi(\boldsymbol{U}, \boldsymbol{\alpha}) = \sum_{m=1}^{N} \sum_{k=1}^{K} (u_{mk})^p (D_{mk})^2 + \sum_{m=1}^{N} \alpha_m \left(\sum_{k=1}^{K} u_{mk} - 1 \right) \tag{2.10}$$

Here, $\boldsymbol{U} = [u_{1,1}...u_{NK}]$ denotes all possible membership coefficients and $\boldsymbol{\alpha} = [\alpha_1...\alpha_N]$ denotes all possible Lagrange multipliers. To minimize this objective function, the gradient with respect to $\boldsymbol{U}$, so each u_{mk} and $\boldsymbol{\alpha}$, so each α_m, must be zero, so:

$$\frac{\partial \Phi}{\partial \alpha_m} = \left(\sum_{k=1}^{K} u_{mk} - 1 \right) = 0 \tag{2.11}$$

$$\frac{\partial \Phi}{\partial u_{mk}} = p(u_{mk})^{p-1} (D_{mk})^2 + \alpha_m = 0 \tag{2.12}$$

Equation 2.11 is the constraint we determined beforehand. Equation 2.12 leads to an expression of the membership coefficient u_{mk}:

$$u_{mk} = \left(\frac{-\alpha_m}{(D_{mk})^2} \right)^{1/(p-1)} \tag{2.13}$$

Substituting k for j and sum over $j = 1...K$ gives:

$$\sum_{j=1}^{K} u_{mj} = \sum_{j=1}^{K} \left(\frac{-\alpha_m}{(D_{mj})^2} \right)^{1/(p-1)} = 1 \tag{2.14}$$

We can rewrite Equation 2.14 by taking α_m out of the sum, which means:

$$(-\alpha_m)^{1/(p-1)} = \left(\frac{1}{\sum_{j=1}^{K} \frac{1}{(D_{mj})^2}} \right)^{1/(p-1)} \tag{2.15}$$

$$-\alpha_m = \left(\frac{1}{\sum_{j=1}^{K} \frac{1}{(D_{mj})^2}} \right) \tag{2.16}$$

Using this definition of α in 2.13 gives:

$$u_{mk} = \left(\frac{\left(\frac{1}{\sum_{j=1}^{K} \frac{1}{\left(D_{mj}\right)^2}} \right)}{\left(D_{mk}\right)^2} \right)^{1/(p-1)} \tag{2.17}$$

Since D_{mk} does not depend on j, it can be taken inside the sum of Equation 2.17, resulting in the equation for the membership coefficients used in the algorithm.

$$u_{mk} = \left(\frac{1}{\sum_{j=1}^{K} \frac{(D_{mk})^2}{(D_{mj})^2}} \right)^{1/(p-1)} = \left(\sum_{j=1}^{K} \left(D_{mk}/D_{mj}\right)^{2/(p-1)} \right)^{-1} \tag{2.18}$$

2.2. Finite Time Lyapunov Exponent

2.2.1. Advected gradient and particle cluster method

The Finite Time Lyapunov Exponent, or FTLE, as described in Chapter 1, is a measure of fluid parcel separation in a turbulent flow. One of the most important steps in calculating the FTLE is the determination of the flow map gradient $\nabla F_{t_0}^{t_1}$. Although it is mathematically defined by an integration of velocity gradients in a velocity, both Shadden and Haller [11] [20] use a discrete method to calculate the flow map gradient $\nabla F_{t_0}^{t_1}$, which is based on following a cluster of virtual particles in the flow and find the separation of these particles over time. Finding the flow map by integrating velocity gradients will be called the "Advected Gradient Method", while the more discrete method will be called the "Particle Cluster Method". Haller [11] claims that the Particle Cluster Method leads to less noisy results, which will be verified here.

The flow map gradient in the Advected Gradient Method makes use of the fact that the flow map gradient $\nabla F_{t_0}^{t_1}$ at initial location (x_0, y_0) at starting time t_0 is a fundamental solution of Equation 2.19,

$$\frac{d\vec{\delta}}{dt} = \vec{\delta} \cdot \nabla \vec{u} \tag{2.19}$$

where $\vec{\delta}$ is an infinitesimally small separation of fluid across the path of a fluid parcel and $\nabla \vec{u}$ is the gradient of the velocity field. The formal solution of this equation is:

$$\delta(t + \Delta t) = e^{\left(\int_t^{t+\Delta t} \nabla u(t\prime) dt\prime\right)} \delta(t) \tag{2.20}$$

which defines the flow map gradient as:

$$\delta(t_1) = \nabla F_{t_0}^{t_1} \delta(t_0) \tag{2.21}$$

The Particle Cluster Method calculates $\nabla F_{t_0}^{t_1}$ differently. This method makes a grid of points a starting time t_0, each on a location (x_0, y_0). Next, extra particles are introduced exactly north, east, south and west of each particle with a certain Δx and Δy. Following these 4 extra particles around the particle that started on (x_0, y_0) from t_0 to t_1 results in a flow map around (x_0, y_0). With the initial distances between the north, south, east and west particle taken into account, the flow map gradient $\nabla F_{t_0}^{t_1}$ can be calculated by:

$$\nabla F_{t_0}^{t_1}(x_0, y_0) = \begin{bmatrix} \frac{x_1(x_0+\Delta x, y_0) - x_1(x_0-\Delta x, y_0)}{x_0(x_0+\Delta x, y_0) - x_0(x_0-\Delta x, y_0)} & \frac{x_1(x_0, y_0+\Delta y) - x_1(x_0, y_0-\Delta y)}{y_0(x_0, y_0+\Delta y) - y_0(x_0, y_0-\Delta y)} \\ \frac{y_1(x_0+\Delta x, y_0) - y_1(x_0-\Delta x, y_0)}{x_0(x_0+\Delta x, y_0) - x_0(x_0-\Delta x, y_0)} & \frac{y_1(x_0, y_0+\Delta y) - y_1(x_0, y_0-\Delta y)}{y_0(x_0, y_0+\Delta y) - y_0(x_0, y_0-\Delta y)} \end{bmatrix} \tag{2.22}$$

Here $x_1(x_0, y_0)$ denotes the x-location at time t_1 of the particle that started at (x_0, y_0) at the initial time t_0. The difference in calculating between these two methods is visualized in Figure 2.3. Using both methods, an FTLE-field is calculated for a test measurement. The difference between the results of the two methods can be found in Figure 2.4. This figure shows that both methods produce approximately the same field, as in both fields the same structures can be identified. As Haller [11] claimed it is shown that the Particle Cluster Method gives a much clearer and more smooth result for the FTLE-field compared to the Advected Gradient Method. Therefore, this method will be used to calculate the FTLE in the remainder of this thesis.

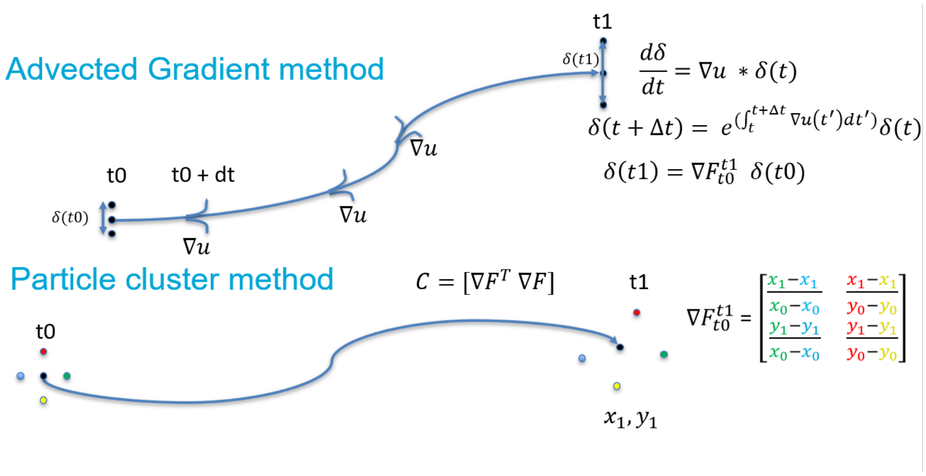

Figure 2.3: Schematic explanation of two different methods to calculate the flow map gradient needed for the FTLE. Above: The gradient is calculated along a virtual particle path, integrating leads to the flow map gradient. Below: the path of a cluster of particles is followed to determine the flow map gradient.

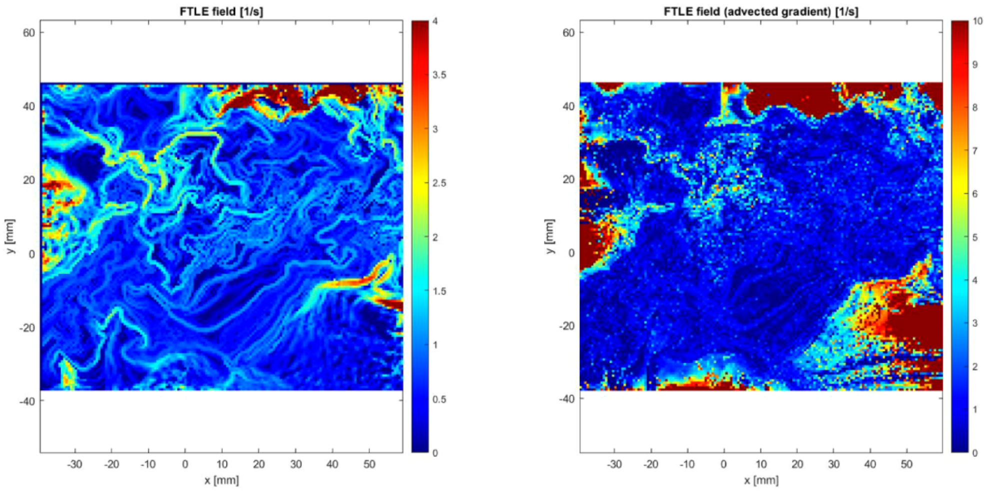

Figure 2.4: Left: An FTLE-Field using the particle cluster method. Right: The same FTLE-field using the advected gradient method. The same structures are visible in the middle of the field, but at the edges the advected gradient method is more noisy and structures are harder to distinguish.

2.2.2. The FTLE-algorithm

An algorithm is implemented to calculate the FTLE-field. First, the velocity-fields of a whole measurement, including x- and y-locations of the vectors, are loaded altogether. Next, a matrix of virtual particles is introduced on the same locations as the velocity vectors. The particles will be advected by the flow field. The resolution of this matrix can be increased by introducing a finer matrix of particles, of which the positions and initial velocities positions can be interpolated. For both the forward (+) and backward (-) time FTLE, these particles are advected by:

$$x_{new} = x_{old} \pm u\Delta t \tag{2.23}$$

$$y_{new} = y_{old} \pm v\Delta t \tag{2.24}$$

where x_{new} and y_{new} are the respective x- and y-location of the particles that were located at (x_{old}, y_{old}) at the previous time step, u and v are the velocities of the old time step in x- and y-direction respectively and Δt is the time step between the two velocity fields

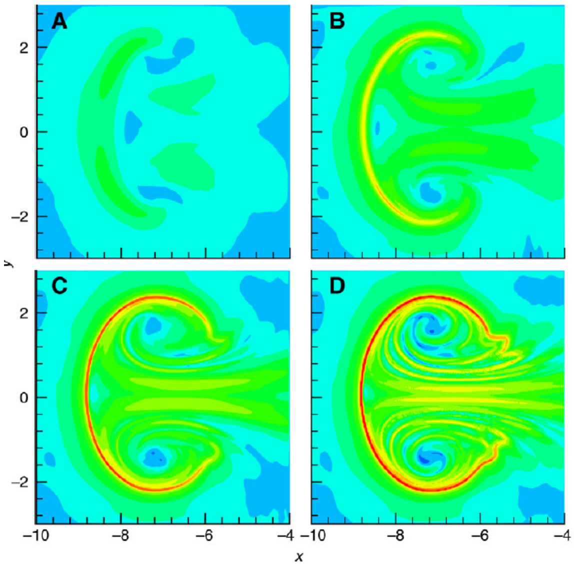

Figure 2.5: The effect of integration time on FTLE (Finite Time Lyapunov Exponent) and LCS (Lagrangian Coherent Structure) calculation for a vortex ring. (A) integration time $T_i = 0.4$ s; (B) $T_i = 1.2$ s; (C) $T_i = 2.0$ s; (D) $T_i = 2.8$ s. With longer integration time, the FTLE ridges become sharper, i.e. LCS resolve into clearly defined thin lines. (adopted from Peng [17])

This brings all particles at a different location for the next time step, so to find their new velocity at this next time step, the velocity field must be interpolated for all new particle positions. When this is done, the particles are advected again by Equations 2.23 and 2.24. This whole procedure is repeated until a pre-selected number of time steps is reached, or is stopped for individual particles if they leave the field-of-view. From their final positions at t, a flow map gradient $\nabla F_{t_0}^t(\boldsymbol{x_0})$ from the initial positions at t_0 can be made with equation 2.22. With this flow map gradient the Cauchy-Green Tensor can be calculated with equation 2.25, and then, with the corresponding t, the FTLE for each position can be calculated via equation 2.26.

$$C(\boldsymbol{x_0}) = [\nabla F_{t_0}^t(\boldsymbol{x_0})]^T \nabla F_{t_0}^t(\boldsymbol{x_0}) \tag{2.25}$$

$$\sigma_{t_0}^t(\boldsymbol{x_0}) = \frac{1}{2|t-t_0|} \log(\lambda_{max}(\boldsymbol{x_0})) \tag{2.26}$$

With λ_{max} the highest eigenvalue of the Cauchy-Green strain tensor. The $T_i = (t - t_0)$ in Equation 2.26 is an important parameter, called the integration or observation time. This parameter is determined by the time a complete cluster of particles is in the field-of-view. It is desirable to make this integration time as high as possible, because increasing this makes the LCSs much sharper and therefore much easier to observe, as is shown more clearly in Figure 2.5. A schematic description of this algorithm can be found in Figure 2.6.

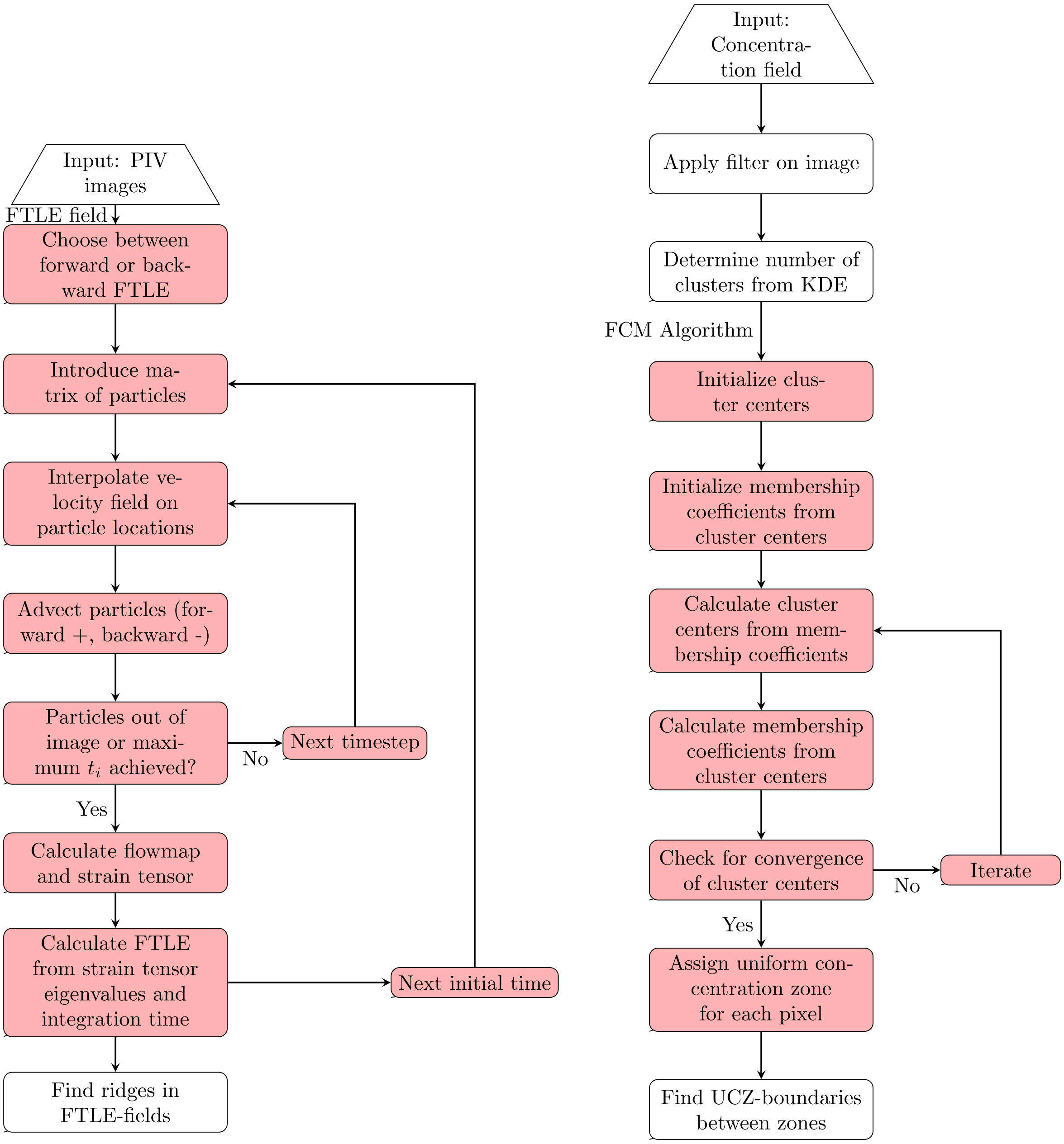

Figure 2.6: The algorithms to find UCZs and the FTLE. The steps in red describe the actual algorithm, the white steps are preparation or post-processing. Left: Pseudocode of FTLE-algorithm. Right: Pseudocode of the FCM-algorithm

3

Parameter study

The proposed experiment consists of Lagrangian PIV-measurements (and later also LIF-measurements) on an axisymmetric turbulent jet from a small nozzle in a large water tank. Instead of a fixed camera, the camera, and therefore our field of view, will follow the flow with a velocity U_C using a traverse mechanism. In this chapter, the design parameters of an ideal scenario of the experiment are discussed first. Next, calculations on how the jet is built using an overflowing barrel principle are done and finally the design parameters of the actual experiment are chosen following a design envelope with realistic constraints.

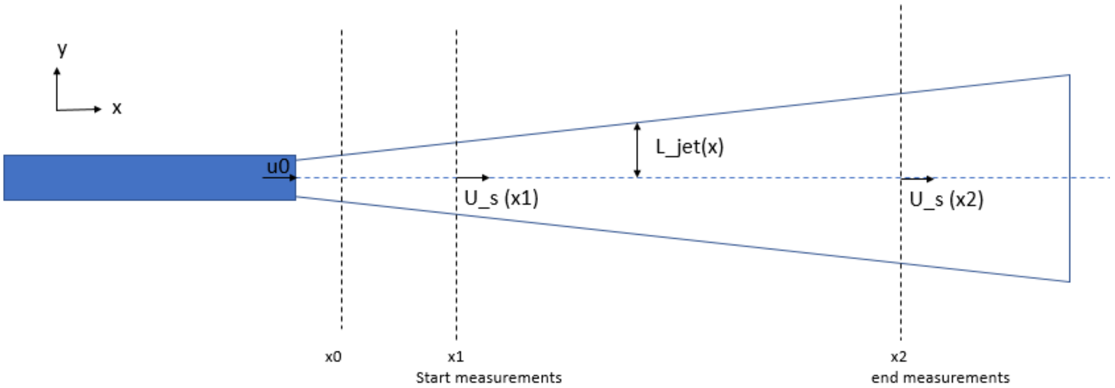

Figure 3.1: Schematic view of the Jet

3.1. Ideal scenario

In order to observe the desired Lagrangian Coherent Structures, we propose a PIV-experiment with moving cameras along a turbulent jet. The goal is to keep different turbulent length scales in our field-of-view for a longer time than with a fixed camera. The design of such an experimental setup is not straightforward, since the size of turbulent length scales depend on the inlet conditions of the jet and increase further away from the inlet. The experiment will be designed in such a way that at the beginning of the measurements the resolution is equal to the turbulent microscale in the jet. The end of the measurements is defined as the location where the turbulent macroscale of the jet equals the whole field-of-view. A schematic view of the jet is given in Figure 3.1.

3.1.1. Inlet conditions

Most of the properties inside a turbulent jet, such as length scales and local (averaged) velocities, are determined by the Reynolds number:

$$Re = \frac{UL}{\nu} \tag{3.1}$$

where, U is a velocity scale, L is a length scale and ν is the kinematic viscosity of the fluid. In water $\nu = 1\times10^{-6}$. The Reynolds number inside a turbulent jet is constant, according to Nieuwstadt et al. [16], and is determined by the Reynolds number at the nozzle. With a nozzle diameter and outlet velocity of respectively $d = 1mm$ and $U_0 = 2m/s$, the Reynolds number is equal to 2000. This is a relatively low Reynolds number to make sure that the ratio between macro- and microscales in the jet is relatively small. This allows us to capture both scales in our field of view for as long as possible. These inlet conditions also match the experiments of Westerweel et al.[25], to validate the found results later.

3.1.2. Field-of-view and camera

The starting point of the measurement x_1 is set at $0.15m$ from x_0, where x_0 is estimated to be 6.8 mm from the nozzle outlet, according to Nieuwstadt et al. [16]. The mean centerline velocity, which is where the velocity is the highest for a given x-location, is given by equation 3.2, from Nieuwstadt et al. [16].

$$\frac{U_s}{U_0} = \frac{B_U d}{x - x_0} \tag{3.2}$$

with the decay parameter $B_U = 6.7$ given by Boersma et al. [4]. At $x_1 - x_0 = 0.15$, this mean centerline velocity U_s is equal to $0.0893m/s$. This way, the chosen centerline velocity U_S at x_1 is not beyond the limitations of the traverse mechanism in x-direction ($U_C < 0.115$), so the traverse mechanism is able to follow the flow.

This starting location determines the smallest scales we need to consider. In a fully developed turbulent jet, the turbulence characteristic quantities depend on the velocity and distance to the (virtual) origin of the jet. The smallest scale we consider here is the Taylor microscale (λ_T). Westerweel et al. [25] finds the Taylor microscale (λ_T) from calculating the turbulent dissipation ϵ:

$$\epsilon = 0.015\frac{U_s^3}{l} \tag{3.3}$$

$$\epsilon = 15\nu\frac{(u')^2}{\lambda_t^2} \tag{3.4}$$

Here, U_s is the local centerline velocity, l is the macroscale, calculated in Equation 3.5, u' is the average fluctuation velocity, which is equal to $0.25U_s$ and ν is the kinematic viscosity of water, which is $1\times10^{-6}m^2/s$

At x_1, the dissipation is equal to $0.00074m^2/s^3$ and the Taylor microscale is equal to 3.2 mm. This value should also be the length and width of the interrogation window in the PIV-images. With the interrogation window set at 32x32 pixels, the length of one pixel l_{pix} must be $0.1mm$. The macroscales in the jet are given by the velocity half width of the jet, which is given by Equation 3.5.

$$l = 0.0965(x - x_0) \tag{3.5}$$

The resolution of the camera with the pixel size determines the largest macroscale that can be recorded by the camera. Assuming we use a 5 MP camera with approximately 2200 pixels in length and width and a camera pixel size $l_{pix,cam} = 7\mu m$, this will correspond with a largest macroscale of $l = 0.22m$. Therefore, the needed magnification is:

$$M_0 = \frac{l_{pix,cam}}{l_{pix}} = \frac{7\times10^{-6}}{0.1\times10^{-3}} = 0.07 \tag{3.6}$$

The largest macroscale determines the location in the jet where we can still measure the macroscale and therefore the end-location of the measurement area x_2. Solving 3.5 for x, where $l = 0.22m$, results in $x_2 - x_0 = 2.28m$. Velocity data and length scales on both x_1 and x_2 are found in Tables 3.1 and 3.2

Table 3.1: Mean and fluctuation velocity at the centerline and mean velocity at the halfwidth and turbulent boundary at the start and end location of the experiment. The jet boundary is determined by $L_{Jet} = 1.99l(x)$, according to Westerweel et al. [25]

	U_s	U_{RMS}	$\bar{U}$ (Boundary)	$\bar{U}$ (Half width)
$x_1 = 0.15m$	$0.0893m/s$	$0.0223m/s$	$0.0128m/s$	$0.0447m/s$
$x_2 = 2.28m$	$0.0059m/s$	$0.0015m/s$	$0.00085m/s$	$0.0029m/s$

Table 3.2: Micro scale, halfwidth (which is also used as macroscale), jet boundary and integral length scale at start and end location of the experiment. The jet boundary is determined by $L_{Jet} = 1.99l(x)$, according to Westerweel et al. [25]

	λ_T	$l(x)$	L_{jet}
$x_1 = 0.15m$	$3.2 \times 10^{-3}m$	$0.0145m$	$0.029m$
$x_2 = 2.28m$	$12 \times 10^{-3}m$	$0.22m$	$0.44m$

The thickness of the interrogation window Δz is 0.5 mm, a common value. For all particles to be into focus, this Δz must be smaller than the depth of the field, δz, which is given by 3.7, from Adrian and Westerweel [1]. With a magnification M_0 of 0.07 and f equal to 11, δz is much higher than 0.5 mm.

$$\delta z = 4\left(1 + \frac{1}{M_0^2}\right)^2 f^2 \lambda \tag{3.7}$$

3.1.3. Particle size and concentration

It is preferred that the particle size of the seeding is slightly larger than the pixel size, so the exact location of the centerpoint of each particle can be determined from multiple pixels. For this reason the particle size should be $150\mu m$.

According to Adrian and Westerweel [1], the images from the PIV-experiment are valid if there are enough particles, approximately 5 to 7, in every interrogation window, which is given by the image density, Also, there should be enough space between particles in every image, to prevent overlapping of particles in the images. No overlapping of particles is achieved when the source density is small enough, so $N_S << 1$. These densities are given by:

$$N_S = C\Delta z_0 \frac{\pi d_\tau^2}{4M_0^2} \tag{3.8}$$

$$N_I = \frac{CA_I\Delta z_0}{M_0^2} \tag{3.9}$$

Setting N_I at 7 results in a particle concentration of approximately $1.3 \times 10^9 m^{-3}$. At this concentration, the source density $N_S = 3.96 \times 10^{-2}$, so well below 1. The volume fraction of particles $\phi = 0.00201$. The in-plane loss of pairs will be negligible, since we move along with the flow and therefore (almost) no particles will move out of their windows. The out-of-plane loss of pairs is used to constrain Δt, by using the "one quarter rule" in 3.10.

$$\frac{|w_{max}|\Delta t}{\Delta z_0} < 0.25 \tag{3.10}$$

The (fluctuation) velocity out of the plane $|w|_{max}$ has its maximum at the centerline and is equal to approximately $0.25U_s$. This means that the highest value of this velocity is at x_1 and is equal to $0.0223m/s$. This means that Δt between pulses must be lower than $0.0056s$.

3.2. Measurement time and Velocity profile

The centerline velocity decreases with increasing x, following equation 3.2. The question is how long we can follow a turbulent fluid parcel as we move the camera from x_1 to x_2, where x_1 and x_2 are determined in section 3.1.2. Then:

$$\Delta t = \int_{t1}^{t2} dt = \int_{x_1}^{x2} \frac{dt}{dx} dx = \int_{x_1}^{x2} \frac{1}{U_s(x)} dx \tag{3.11}$$

so that

$$\Delta t = \frac{1}{2U_0 B_U d}\left((x_2 - x_0)^2 - (x_1 - x_0)^2\right) \tag{3.12}$$

with $x_2 = 2.28m$ and $x_1 = 0.15m$, $\Delta t = 193s$. This seems like a very long time, but this is caused by the fact that the centerline velocity is very low around x_2, that is $0.0059m/s$, so if we follow the flow exactly the last part is very slow. If the camera moves along with the flow with a constant velocity U_C, we simply take the average velocity:

$$U_C = \frac{x_2 - x_1}{\Delta t} \tag{3.13}$$

with $x_2 = 2.28m$ and $x_1 = 0.15m$, it follows that $\Delta t = 193s$ and $U_C = 0.011m/s$. In a more refined experiment U_C should be time dependent and slow down near the end of the measurement area, so further away from the nozzle.

3.3. Jet design

To achieve the proposed Reynolds numbers from the previous section, the jet must be designed in such a way that for a given nozzle diameter, the outlet velocity is constant and at a value that results in the desired Reynolds number. These goals will be reached by connecting the nozzle with a pipes and an overflowing barrel, as can be seen schematically in figure 3.2. The overflowing of the barrel gives the barrel a constant water level z_1, which results in a constant velocity out of the jet. The relation between the water level in the barrel and the jet velocity is given by Bernoulli's law with friction losses from White [26]:

$$\frac{p_1}{\rho g} + \frac{\alpha_1 V_1^2}{2g} + z_1 = \frac{p_2}{\rho g} + \frac{\alpha_2 V_2^2}{2g} + z_2 + \Delta h_{tot} \tag{3.14}$$

Because of hydrostatic pressure, p_2 is slightly higher than p_1 (which is atmospheric pressure) and the velocity at the air-water interface of the barrel, V_1 is considered to be zero. The design parameters can be found in table 3.3. The values of the kinetic energy correction factors $\alpha 1$ and α_2 can be assumed to be 1.06. The total head loss, Δh_{tot}, consists of the loss of pressure due to friction in the pipe and tube, h_f and the minor losses in the system, caused by the connection from the barrel to the valve, the valve itself, the bends in the pipe and the nozzle, which is Σh_m.

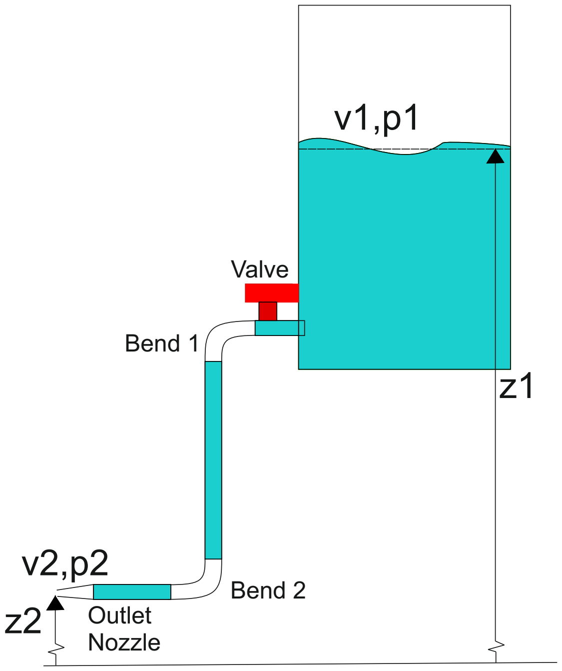

Figure 3.2: Schematic figure of the setup for the jet, with the height (z), velocity (V) and pressure (p) at water level in the tank (1) and at the nozzle outlet (2)

$$\Delta h_{tot} = h_f + \Delta h_m = \frac{V^2}{2g}\left(\left(\frac{fL}{d}\right)_{pipe} + \Sigma K\right) \tag{3.15}$$

The values of the friction factors f and the minor losses K are calculated from tables and diagrams in [26]. The friction factor in the pipe is equal to 0.04 and the other losses are given in Table 3.4.

Because we need to know the required water height in the barrel for specific outlet velocities, 3.14 can be written as:

$$z_1 = \frac{p_2 - p_1}{\rho g} + \frac{\alpha_2 V_2^2}{2g} + z_2 + \Delta h_{tot} \tag{3.16}$$

Using the data from Tables 3.3 and 3.4 in Equation 3.16, an outlet Reynolds number of 5000 leads to $z_1 = 0.69m$ and a Reynolds number of 10000 leads to $z_1 = 0.94m$. The Reynolds number of 5000 and 10000 are found by assuming a nozzle of 5 mm and a nozzle outlet velocity U_0 of respectively 1 and 2 m/s. Since the pipe has a diameter of 10 mm, the velocity through the pipe is 0.25 and 0.5 m/s respectively.

Table 3.3: Design parameters of the jet for $Re = 5000$

Parameter	Value
Jet height z_2	$0.27m$
Water height z_w	$0.6m$
Outlet velocity V_2	$1m/s$
Nozzle diameter d_2	$0.005m$
Pipe diameter d_{pipe}	$0.01m$
Pipe length L_{pipe}	$0.6m$

Table 3.4: K-values of minor losses in the system

Loss	K
Entrance from barrel	0.5
Valve (Estimated)	5
Bend 1	0.4
Bend 2	0.4
Nozzle	0.02
Exit	1
Total of minor losses	7.32

3.4. Design Envelope

The parameters from the section 3.1 give an insight about how the the experimental setup should be formed in an ideal scenario. The actual situation is, naturally, not entirely ideal, because some limitations of the setup in the laboratory lead to constraints in the setup design. This section describes these constraints and gives an overview for what design variables (Reynolds number, image magnification, etc.) the setup is suited and gives the decision in how the final experiments should be designed.

3.4.1. Constraints

The setup, as we will build it, has some preliminary constraints that we need to consider before building it. These constraints include:

- Water tunnel: the water tunnel we can make use of is already built in the laboratory, so we are constrained by the size of this tunnel, which is 60x60x500 cm. This means we have to consider the part of the jet that is not influenced by the walls of the tunnel or the water surface at the top of the tank.
- Traverse mechanism: as discussed earlier, the traverse mechanism has a maximum horizontal velocity of $0.1155 m/s$. If we want to follow the stream carefully, we should consider the part of the jet that has a velocity smaller than $0.1155 m/s$.
- Camera position: we can not put the traverse with the camera under water, so it is placed outside of the water tunnel. Since the centerline of the jet is in the middle of the tunnel, the camera or lens must be placed at least $30cm$ from this centerline ($Z_0 > 30cm$), with a maximum of $2m$ to fit in the laboratory. This means, with the available camera lens(es), the magnification of the image (M_0) will have a certain range in which we can operate.
- Laser sheet: The available lenses for the laser can make a suitable laser sheet with a width of approximately $70cm$.

The precise (numerical) implications for the setup of these constraints will be discussed in the next section.

3.4.2. Design variables

The final setup has three important design variables, which are limited by the constraints of the previous sections. These design parameters are:

- Magnification: The magnification is constrained by the camera position. The distance from the available lens to the camera (z_0) is $105mm$. With $Z_{0,min} = 300mm$ and $Z_{0,max} = 2000mm$, the magnification range is given by:

$$M_{0,max} = \frac{z_0}{Z_{0,min}} = 0.35 \tag{3.17}$$

$$M_{0,min} = \frac{z_0}{Z_{0,max}} = 0.053 \tag{3.18}$$

- Reynolds number: Since the centerline velocity of the jet is proportional the Reynolds number, see Equation 3.2, both the nozzle diameter and the outlet velocity could be varied to change the Reynolds number of the jet. Therefore, both nozzle size and outlet velocity will be put together in one variable.

The Reynolds number will be limited by the size of the water tunnel and laminar-to-turbulent transition of the jet. If Re is very high, in the order of 10^5, the jet will hit the wall before the centerline velocity is below $0.11 m/s$, so there is no possible point to follow an undisturbed jet. Also the Reynolds number must be high enough for the jet to be turbulent. The laminar-to-turbulent transition of a jet occurs around $Re = 2000$.

- Measurement area: the measurement area is defined by the small turbulent microscale at the start of the measurement area (x_1) and by the macroscale at the end of the measurement area (x_2). It is preferred to have the small scales at the size of at least one interrogation window, so 32 pixels in the image. The macroscale must always fit into the image, so the length of approximately 2200 pixels must be larger than the largest scales in the jet. The required pixel size that is needed for this must be feasible with the constrained magnification.

3.4.3. Determining parameters

Here the design parameters of the final experimental setup are chosen. It is seen in section 3.1 that the Taylor microscale is not much smaller than the macroscale in the case where $Re = 2000$, which results in a very large possible measurement area, which is not feasible in the water tunnel. Therefore, three other candidates are introduced here to act as the spatial resolution in the experiments: the Kolmogorov scale, 4 times the Kolmogorov scale and 6 times the Kolmogorov scale. The Kolmogorov scale is a candidate because this is the smallest length scale in turbulent flows, calculated by:

$$\eta = \left(\frac{\nu^3}{\epsilon}\right)^{0.25} \tag{3.19}$$

with kinematic viscosity given by ν and turbulent dissipation given by ϵ. According to Westerweel et al. [25], velocity measurements can be considered as fully resolved when the spatial resolution of the data is between 4 and 5 times the Kolmogorov scale. This means that 6 times the Kolmogorov scale is slightly outside of this range, but still a feasible option.

Figure 3.3 shows how the three major design variables (Magnification, Reynolds number, Measurement area) depend on each other and on the set constraints, for all 4 optional small scales as spatial resolution. From Figure 3.3 it is clear that both the Taylor microscale and the Kolmogorov scale are unfeasible for basically all Reynolds numbers, since they fall outside of the constraint along the whole range of Reynolds numbers. Also, the constraint on x_2 based on the length of the water tunnel results in the fact that the Reynolds number should not be higher than 10000, because this significantly shrinks our measurement area, which is undesirable, since we want this measurement area to be as long as possible to keep the fluid longer in our field of view.

According to Figure 3.3, both 4 and 6 times the Kolmogorov length give suitable design variables for Reynolds numbers between 5000 and 10000 with respect to the set constraints. The left part of Figure 3.3 should be read as follows: The thick blue line indicates the start of the measurements x_1, which is a linear function of the Reynolds number and is the location where the mean centerline velocity is equal to $0.1155 m/s$. This location determines the magnification (and pixel size) of the image: we want the small scale to be equal to one interrogation window of 32x32 pixels. Different options of this small scale lead to different magnifications, as shown by the right part of Figure 3.3. The end of the measurements x_2 is determined by the macroscale l, because we want this macroscale to always fit in the image. In other words, x_2 is the location where l equals the size of the whole image, so 2200 pixels. This value of x_2 is showed in different colours for different magnifications, corresponding with the different small scale options, in the left part of Figure 3.3. The dashed lines show maximum values of x_2, given by the length of the laser sheet and the size of the water tunnel. Because choosing 6 times the Kolmogorov length results in a higher x_2, in other words: a larger

Table 3.5: Design variables for the experiment

Variable	Value
Re [-]	5000
Start of measurement x_1 [m]	0.29
End of measurement x_2 [m]	0.80
Magnification M_0 [-]	0.185
Lens distance from the center of the jet Z_0 [m]	0.57

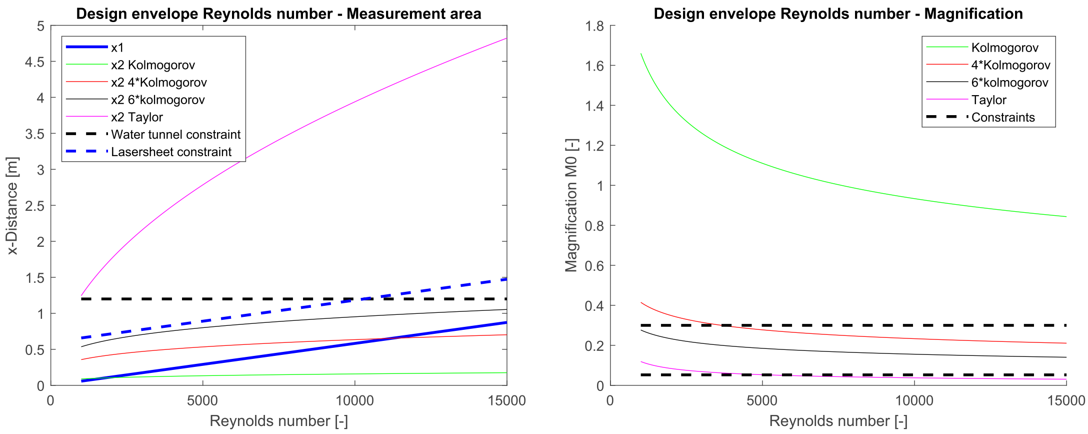

Figure 3.3: Graphical interpretation of the design variables of the experiment. Left: The dimensions of the measurement area for different Reynolds numbers. The thick blue line indicates the start of the measurement area x_1, which only depends on the Reynolds number. The dashed lines indicate the maximum value of the end of the measurement area x_2, constrained by the size of the water tunnel (black) and the size of the laser sheet (blue). The coloured lines each indicate values of the end of the measurement area x_2 for different options of the size of the spatial resolution at x_1. Right: The magnification needed for the spatial resolution to be equal to the four length scale options. The magnification is constrained by the possible camera distance, here indicated by the black dashed line. The four possible length scales are again indicated by the coloured lines.

measurement area, this is chosen to be equal to the spatial resolution at x_1, this is the most suitable option. The largest measurement area is found at approximately $Re = 5000$, which results in the design variables of Table 3.5 and velocities and length scales of Tables 3.6 and 3.7

Table 3.6: Mean and fluctuation velocity at the centerline and mean velocity at the halfwidth and turbulent boundary at the start and end location of the experiment. The jet boundary is determined by $L_{Jet} = 1.99l(x)$, according to Westerweel et al. [25]

	U_s	U_{RMS}	$\bar{U}$ (Boundary)	$\bar{U}$ (Half width)
$x_1 = 0.29m$	$0.1155m/s$	$0.0289m/s$	$0.0166m/s$	$0.0578m/s$
$x_2 = 0.80m$	$0.042m/s$	$0.0105m/s$	$0.006m/s$	$0.0209m/s$

Table 3.7: 6 times the Kolmogorov length scale η, halfwidth (which is also used as macroscale), jet boundary and integral length scale at start and end location of the experiment. The jet boundary is determined by $L_{Jet} = 1.99l(x)$, according to Westerweel et al. [25]

	6η	$l(x)$	L_{jet}
$x_1 = 0.29m$	$1.1 \times 10^{-3}m$	$0.028m$	$0.056m$
$x_2 = 0.80m$	$3.1 \times 10^{-3}m$	$0.077m$	$0.154m$

Using Equation 3.12 for a Reynolds number of 5000 with the values of Table 3.7, the chosen design variables lead to $\Delta t = 8.3s$. With $x_2 - x_1 = 0.51m$, the constant velocity of the cameras $U_C = 0.061m/s$.

4

Experimental setup

The experimental setup consists of four major subsystems: The turbulent jet inside a water tunnel, the camera connected to a PC with Particle Image Velocimetry (PIV) software, the traverse mechanism for the camera controlled by another PC, and the laser sheet made by a laser and some optics. This chapter describes all these subsystems individually and how these are connected to form the complete experimental setup. Also the way the final experiments are performed is explained.

4.1. Setup

4.1.1. Jet

The experiment is done inside the large water tunnel inside the Aero- and Hydrodynamics Lab at the 3ME-faculty of the TU Delft. This water tunnel has a length of 5 m, a width of 0.6 m and a height of 0.6 m. At the beginning of the tunnel the jet is placed, which consist of a 40 L barrel with a tap on the bottom, which is connected to a copper tube (D = 10 mm) with two 90 degrees elbows, resulting in an S-shape. At the end of the copper tube a nozzle with a 5 mm diameter outlet is placed from which the jet enters the water tank. This nozzle is placed in the center of the water tunnel, so 30 cm from both walls and 33 cm from the bottom of the tank. Both the water tunnel and the barrel are filled with demineralized water seeded with particles (Sphericell, 30 μm), to be able to do PIV-experiments. Also, Rhodamine B is dissolved in the water in the barrel to do concentration measurements via Laser Induced Fluorescence (LIF). This water is supplied to the barrel with a waterpump from a reservoir that rests partly in the water tunnel, fixed to the rest of the setup. To maintain a constant water height, a tube is connected to a drain at 15 cm above the tap to build an overflowing barrel. The height of the tube, but not the drain, can be elevated to increase the constant water level and therefore the nozzle outlet velocity. More on this velocity control can be found in section 4.3.3. For pictures of the jet, see Figure 4.1.

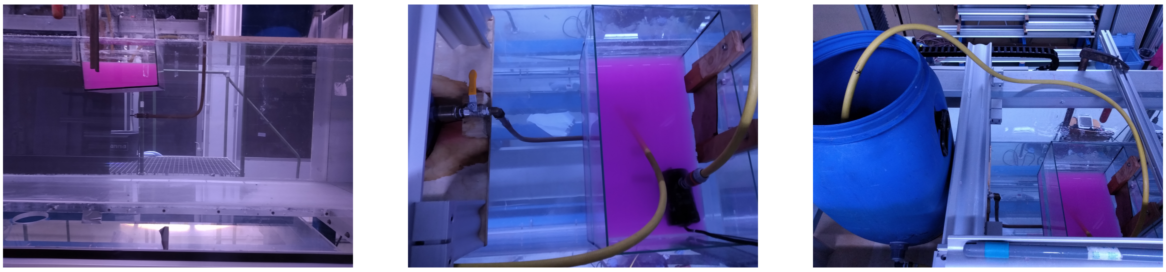

Figure 4.1: Impression of the jet-creating part of the setup. Left: Overview of the jet-system. Middle: Top view of the jet, barrel and reservoir. Right: Side view of the jet, barrel and reservoir

4.1.2. PIV- and LIF-cameras

The measurements are done by two 16-bit, 5 Megapixel ScMos-cameras (LaVision, Göttingen, Germany), controlled by a PC using DAVIS 10. The PIV-camera is equipped with a shortpass filter (> 550nm, FES0550, Thorlabs, Newton, U.S.A.) with a transmission ratio in the rejection region of 0.01% and a 105 mm lens. The LIF camera is also equipped with a 105 mm lens and a longpass filter (< 550nm, FEL0550, Thorlabs, Newton, U.S.A.) with a transmission ratio in the rejection region of 0.01%. Why we chose to use two cameras instead of one is explained in section 4.2. The cameras are connected to the Programmable Timing Unit (PTU), that sends triggers to the camera and the laser, via long optic cables. The cameras, connected to the traverse mechanism, can be seen in Figure 4.2. The lenses of the cameras are placed 34 cm from the glass of the water tunnel, which is equivalent to 64 cm from the nozzle. The LIF-camera is placed 10 cm above the PIV-camera and set under an angle of approximately 3 degrees, to make sure that both cameras capture the same field-of-view.

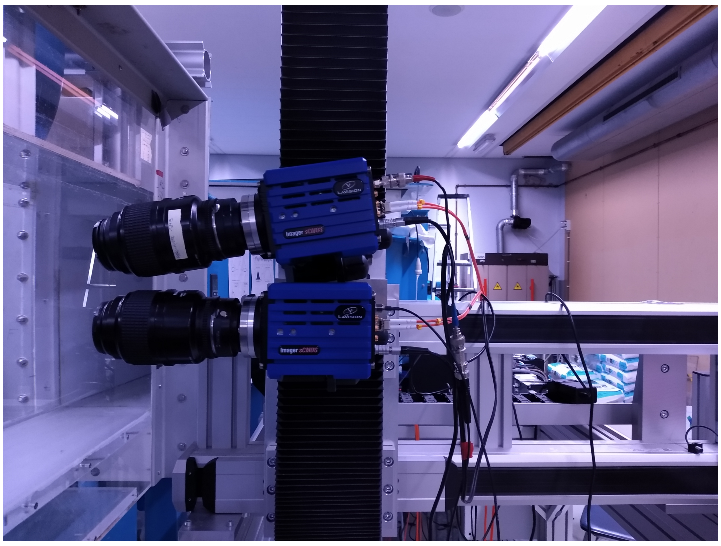

Figure 4.2: Both cameras from close range

4.1.3. Traverse mechanism

The traverse mechanism is a large construction made of three aluminium axes, on which a 18x15 cm endplate can move in three directions. The movement is done by three step motors (MDrive 23 Hybrid, Schneider Electric, Marlborough, U.S.A.) built in the construction, one for each axis. The x-axis, parallel to the jet, is 2 meters long, the y- and z-axis are 1 m long. On the endplate two camera mounts are fixed to hold the two cameras. Each mount has three rotational axes to adjust the cameras' viewing angle. Here, the PIV-camera is set orthogonal to the jet, parallel to the y-axis of the traverse mechanism. The LIF-camera is mounted 10 cm above the PIV-camera, with a downward angle of approximately 3 degrees to have the same field-of-view. The movement is controlled by a Labview program on a different PC than the cameras are connected to. The combination of PC and step motors also provide the triggers to the laser and the cameras at fixed positions during the movement, with a frequency of 10 Hz at constant velocity. For example, if the set velocity is 1 m/s, the traverse will give a trigger every 0.1 m. This means that when the cameras are still accelerating towards this constant velocity, the trigger frequency is lower. This is not a problem, since we established our measurement area to be smaller than 120 cm, so we can use at least 80 cm as a run up area before the measurements start. The whole traverse mechanism can be seen in Figure 4.3.

4.1.4. PC and PTU

The whole setup is controlled and triggered by a PC using DaVis 10 (LaVision, Göttingen, Germany) and a connected Programmable Timing Unit (PTU-X, LaVision, Göttingen, Germany). The PTU receives triggers from the traverse mechanism, at 10 Hz when the cameras have reached constant velocity, and sends triggers to the Q-switch of the laser and cameras, and a second trigger to the PIV-camera a fraction of a second later for the PIV-measurements. The time between these two triggers and the exposure time of the cameras can be set in DaVis, the times used in the final experiments are given in section 4.3.4.

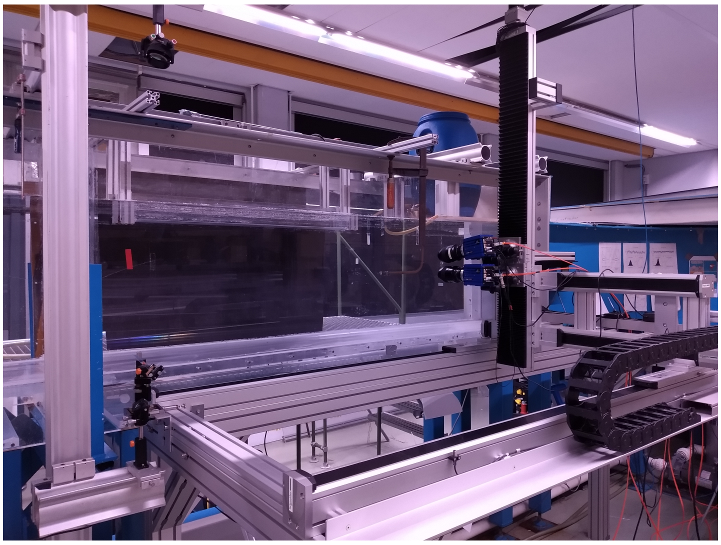

Figure 4.3: Traversing camera setup

4.1.5. Laser

Both the PIV- and LIF measurements are done using the same Double pulsed Nd:YAG laser (Spectra Physics Quanta Ray). The laser is triggered by the aforementioned PTU. The laser is positioned on a table next to and below the water tunnel. In order to get a functional laser sheet inside the water tunnel, the laser beam first has to be directed to the top and the middle of the water tunnel, this is done via two mirrors (Thorlabs, Newton, U.S.A.), see Figure 4.4. To direct the laser into the water tunnel, a third mirror is placed on top of the water tunnel. Right before this mirror, optics are placed to transform the laser beam into a sheet. These optics contain 2 strong cylindrical negative lenses (-25 mm) and one weaker positive lens (1000 mm). This is shown in Figure 4.4, as well as a schematic overview of how the laser sheet is made. After the third mirror, a Plexiglas container is placed exactly on top of the water in the water tunnel. This Plexiglas prevents the laser sheet to be affected by the wavy air-water interface on top op the water tunnel.

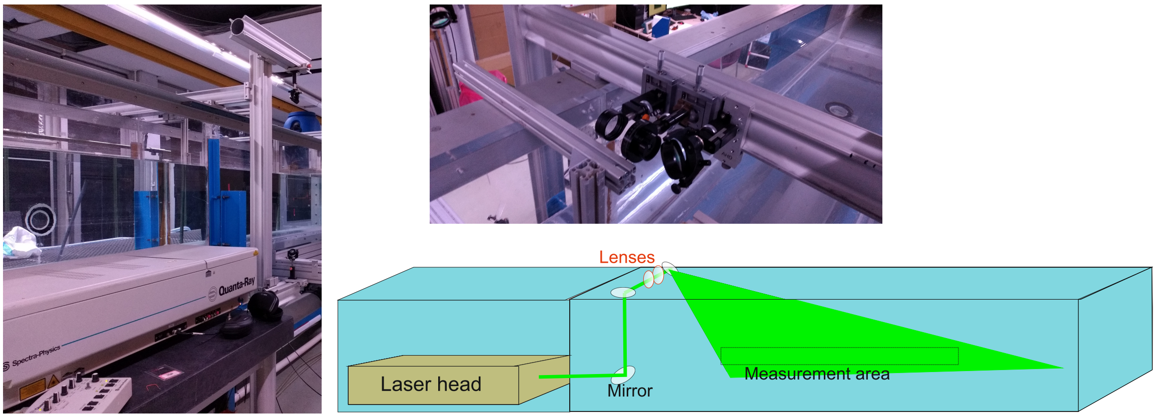

Figure 4.4: Overview of the laser sheet setup. Left: The laser head, followed by the first two mirrors next to the water tunnel. Right bottom: A schematic view of the laser path. Right top: Optics that form the laser sheet. From left to righ: Positive lens (1000mm), 2 negative cylindrical lenses (both - 25mm) and a mirror.

One of the downsides of using only this kind of laser is the fact that there is some variation in laser intensity (approximately 3 percent) during measurements. For PIV-measurements, this is not an issue, because the laser- or image-intensity has negligible impact on the correlations found in the PIV-calculations. For LIF-measurements, this could lead to errors in the measured concentration, since the concentration is directly calculated from image-intensity, which is in principle proportional to the laser intensity. In order to correct the images for this variation in laser intensity, a small piece of microscope glass in placed right after the first mirror. This glass reflects a fraction of the laser beam, which then falls via a polarizing filter on a photo-diode that measures the laser intensity and sends this data to the traverse-PC, see Figure 4.5 for the glass and photo-diode.

Figure 4.5: Setup to measure laser intensity. Left: A mirroring glass after the first regular mirror to reflect a very small part of the laser to the photo-diode. Right: The photo-diode in front of the laser head. Before the laser hits the photo-diode it travels through a polarizing filter

4.2. Separating images

Before the final measurements could be performed, we had to make a decision on whether we would use one camera to make the PIV- and LIF-images simultaneously in the same image and separate the PIV- and LIF-images via numerical filters, or use two cameras and separate the images via physical longpass and shortpass filters. This section describes both methods and justifies the decision to use two cameras.

4.2.1. One camera

Using one camera for both PIV- and LIF-images has some advantages over two cameras. The size of the obtained dataset will be significantly smaller and the installation of one camera is much easier than the installation of two cameras. These are negligible advantages, but the fact that there is only one cameras instead of two, of which at least one is mounted under an angle, results in a more precise and straightforward calibration of position.

A major consequence of using only one camera is that both the PIV-particles as well as the Rhodamine-B used for LIF are captured in the same image. This is not really problematic for PIV-calculations, since the DaVis-software is able to find correlations from the higher light-intensities reflected by the particles with respect to the intensity of Rhodamine-B. However, the presence of particles has a major influence on concentration measurements via LIF. These particles must be filtered out from the images in order to obtain a more reliable concentration field. In an ideal case, the image intensities of the PIV-particles are much higher than those of the Rhodamine, so the images can be separated easily by imposing an intensity threshold. However, this is not the case, so this is only possible by applying for example a median or binomial filter on the image [6, 13]. The results of this filtering on a sample image can be found in Figure 4.6. The filtering shown in Figure 4.6 removes most, but not all, particles from the image, and there is a undesirable loss in resolution, while the image is still grainy.

4.2.2. Two cameras

The other option for separating PIV- and LIF-images is using different cameras for both measurements and using physical wavelength filters to filter the image before it enters the cameras. This is possible because the particles only reflect the light from the laser, therefore the light scattered off the particles for PIV has the same wavelength as the laser (532 nm). The light from the fluorescence of Rhodamine has a larger wavelength (580 nm). This means that a shortpass filter for wavelengths under, for example, 550 nm for the PIV-camera and a longpass filter with the same wavelength for the LIF-camera can split both measurements over two cameras.

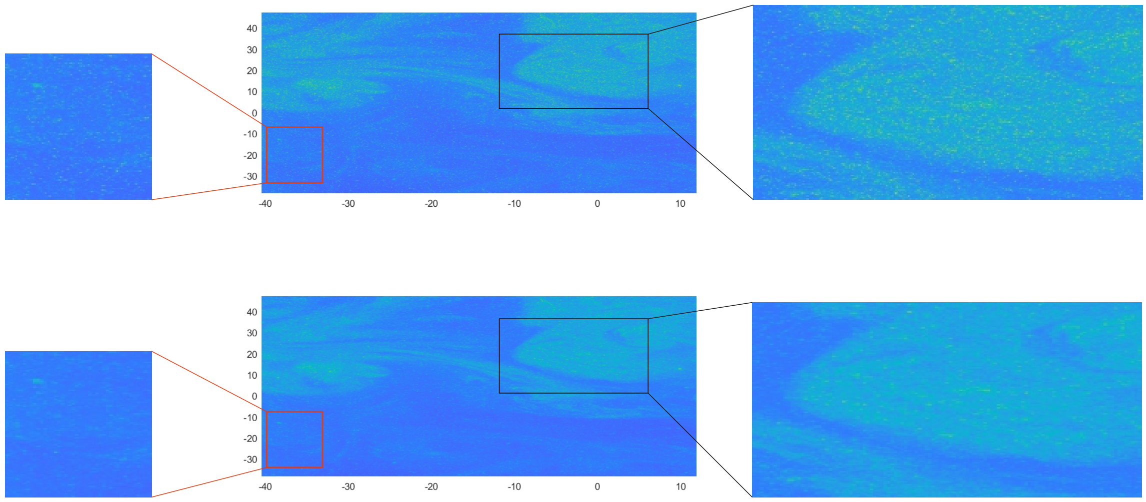

Figure 4.6: Image with LIF and PIV done with one camera. The red and black squares are zoomed in at the sides of the pictures to show the difference. Above: Raw image from camera. Below: Filtered image, but particles are still slightly visible and the image is still grainy.

4.2.3. Conclusion

As long as it is possible in the setup and cameras and filters are available, two cameras are preferred over one camera to separate PIV- and LIF-images. Using only one camera has some advantages in setting up and calibrating the measurements, but these advantages do not compare to the loss in resolution that is caused by filtering the images in post-processing.

4.3. Experimental procedure

This section describes the procedure of how the measurements are done. First, preparations for the measurements, like calibration and the installation of the jet, are described. Then, the way the measurements are done is illustrated. Finally the way the data is structured is explained and the post-processing steps will be discussed.

4.3.1. Preparation

Before we can start the final measurements, a number of steps have to be checked. First, the laser must be switched on for at least 15 minutes before it can be used. During this time, the water levels of the water tunnel (60 cm), the barrel and its reservoir are checked and, if necessary, filled up to the correct level. At this point the pump that circulates the water through the barrel and the reservoir can be switched on. When the laser is warmed up, it is switched at a very low emission level to check whether the laser sheet is still in the proper position, which is parallel to the jet outlet and in the center of the water tunnel and the jet. This laser sheet check is done with the help of the position calibration target, more on this in the next section. If the laser sheet is in the right position, we can shoot some test images to check if the cameras are in focus.

4.3.2. Position calibration

The position calibration is done by placing a target with a known geometric pattern at the measurement location, see Figure 4.7. In our case this is a laser cut black rectangle (610x150 mm) glued on a Plexiglas plate, which has a pattern of white circles engraved in it. The circles are have a diameter of 3 mm and its midpoints are 10 mm apart. This position calibration has two functions: First, making sure that the laser sheet and the focus of the cameras are all positioned at the desired position in the center of the jet. Furthermore, the known pattern can be uploaded in DaVis, which has an built-in algorithm to transform all the raw images using this calibration into images with true x- and y-coordinates in mm.

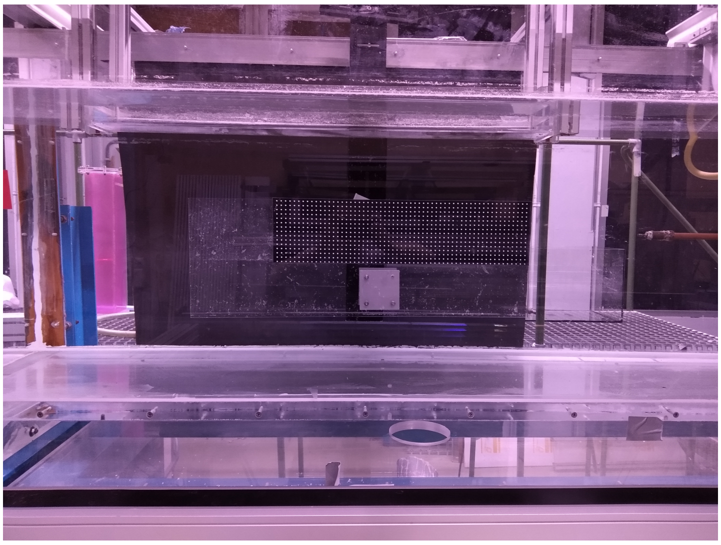

Figure 4.7: Calibration target in the middle of the water tunnel for position calibration

4.3.3. Jet velocity control

The water height, and therefore the velocity is controlled by adjusting the height of the side outlet of the barrel which leads to the reservoir. The outlet itself is fixed, but the tube that connects the barrel to the reservoir can be raised. Since this tube and the barrel are communicating vessels, the highest point of the tube will also be the water level in the barrel. The outlet is located 15 cm above the water level in the tunnel, which is 75 cm above the bottom of the tank. This is a bit higher than the 69 cm that was calculated in the previous chapter, so the Reynolds number of the jet will be higher than planned, probably $Re \approx 6000$. This is merely an estimation, since the friction values of the parts after the barrel, especially the valve, are difficult to determine exactly. Also, the outlet velocity in the current setup is hard to check; this will be discussed in the next chapter. The second part of the measurements, with a higher Reynolds number, was done with a water level of 26 cm above the water tunnel, which corresponds quite well with a Reynolds number of 10000.

4.3.4. Software settings

The measurements are controlled by the DaVis software, which controls the exposure time and time difference between the PIV-Frames. The DaVis settings can be found in Table 4.1. The time difference is slightly too high at the beginning of the measurements, resulting in some filled in vectors where no correlation was found. However, this only occurred at the first couple of frames and resulted in a much lower loss of vectors at the end of the measurements.

Table 4.1: Measurement settings in DaVis while doing the experiment

DaVis variable	Setting
Exposure time PIV-camera	10 µs
Exposure time LIF-camera	2000 µs
dt PIV-camera	8000 µs
Triggering	External random
Number of frames	430
Frequency	10 Hz

4.3.5. Measurement procedure

In total there have been 26 measurement runs at the low Reynolds number and 10 runs at the higher Reynolds number. An impression of how a measurement looks like while measuring can be found in Figure 4.8. This is done in sets of 2 subsequent measurement runs, each at a single Reynolds number. After that the jet is turned off and the whole water tunnel is flushed for approximately 15 minutes to remove all Rhodamine with a UV-filter. Without this procedure, the Rhodamine will build up in the water tunnel, which greatly distorts our measurements. During this time, other aspects of the setup need to be inspected, namely checking whether the reservoir for the jet is full enough to maintain a constant water level in the barrel, removing particles and bubbles from the glass of the water tunnel through which the camera films and from the Plexiglas container where the laser sheet goes through, and checking by eye whether the particle seeding in the water tunnel is sufficient to do new PIV-measurements. If everything is checked and the water tunnel is switched off for some time, the jet can be opened again and new measurements can be done.

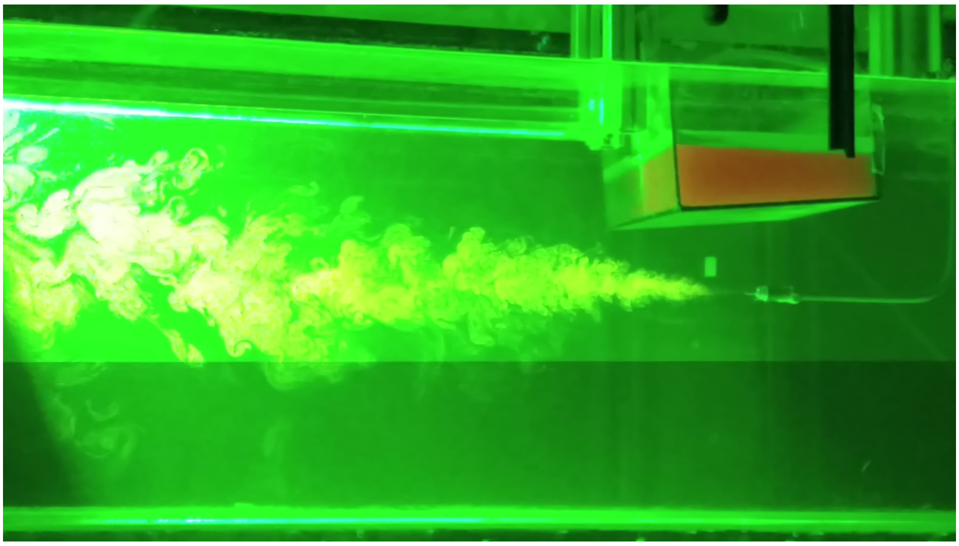

Figure 4.8: Example of the jet during a measurement

4.4. Building the dataset

In total there have been 26 measurement runs at the low Reynolds number and 10 runs at the higher Reynolds number. In between some of the measurements some images are made with a non-moving camera, so we can look at some turbulent statistics in the next chapter.

4.4.1. Useful frames

The traverse needs some time and distance to accelerate to the desired constant velocity. For this reason, a run up is required, where the cameras are already filming but the images will not be used. This run up causes the triggering to be at a non-constant frequency, which was not beneficial for the performance of the laser. To make sure the laser works properly, this run up is made as long as possible. The LIF-images are calibrated for an area of 40 cm (+ one field-of-view), which is started at 36 cm from the zero of the traverse. This way, to calculate the FTLE both forwards and backwards, there is enough room both upstream and downstream to observe particles in the FTLE-alogrithm. The room on both sides is 22 cm, which corresponds with 5.5 seconds of observation time from the most outside points of the useful LIF-images, which is more than enough to find sharp FTLE-ridges. The way the frames are sorted is summarized in Figure 4.9

4.4.2. PIV-images

The processing of the PIV-measurements are done using four passes. On the first pass, the interrogation windows on which the correlations are calculated are 64x64 pixels, with 50% overlap. The last three passes are done on a 32x32 interrogation window, also with 50% overlap. In preprocessing, a min/max filter of 5x5 pixels is applied on the images. There are multiple steps in post processing, which are:

- Delete if peak ratio $Q < 1.1$
- Universal outlier detecting with 1x median filter, with a region of 5x5 vectors
- Remove if residual > 2
- (Re)insert if residual < 3

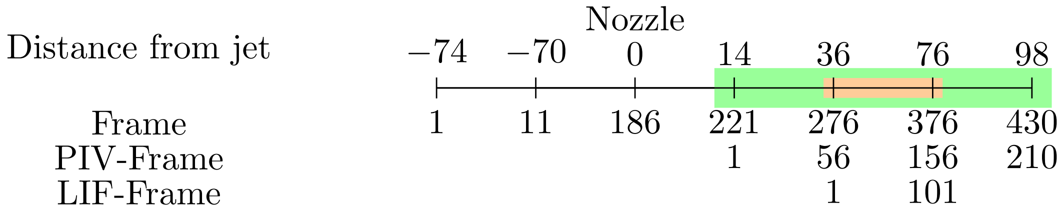

Figure 4.9: Schematic of how the frames are sorted. A whole measurement starts at frame 1 at 74 cm before the nozzle. The 210 PIV-frames (green) start at 22 cm after the nozzle and go to the end of the measurement at 98 cm after the nozzle. The LIF-frames (orange) start at 36 cm after the nozzle and contain 101 frames, which is equal to a travelled distance of 40 cm.

- Miminum number of vectors is 4
- Fill up empty spaces by interpolating

4.4.3. LIF-images

The LIF-images need three relatively small post-processing steps before they are suitable for finding Uniform Concentration Zones. First the useful frames, as in Figure 4.9, are separated from the frames that are not useful for LIF. Then the position calibration is applied on the frames, so the image gets slightly deformed and each pixel receives an x- and y-coordinate. The last step is to convert the image intensity on all locations in all frames to concentration values. This is done by using a calibration matrix or polynomial, which gives a conversion-variable from intensity to concentration given the x- and y-location of the pixel. The calibration procedure that provides this polynomial is described in Section 5.3. After this, some binomial filtering is done to make the concentration images more smooth, but this is only for making the boundaries of the UCZs sharper and is probably not necessary for analysis.

4.4.4. Differences between initial design and actual setup

The actual experimental setup is designed with the design variables of Table 3.5 in mind. However, the real experiment differs slightly from these initial variables. Firstly, the magnification M_0 is slightly bigger than designed, that is $M_0 = 0.194$. This is slightly more zoomed in than designed. As shown in Figure 4.9, the measurement area for PIV-images is goes from $x_1 = 14cm$ from the nozzle to $x_2 = 98cm$ from the nozzle. This is much larger than the initial measurement area, but the surprisingly long length of the laser sheet made it possible to increase the measurement area. However, this means that at respectively the beginning and the end of the measurement area, the proposed small scale and macroscale will not fit exactly in the field-of-view as designed. Especially in at the beginning of the measurement area, the velocities were a bit too high, which resulted in some loss of correlation in the PIV-software. Fortunately, the measurement area is large enough to just ignore the first PIV-frames and still have enough past velocity fields to calculate a backward time FTLE-field that corresponds with the first LIF-frame. The constant velocities at which the cameras move along with the flow is slightly lowered from the initial design, from $U_C = 0.061m/s$ to $U_C = 0.04m/s$. This is a result from test measurements, which showed a significant increase in observation time in the second half of a measurement run, without much loss in the first half of a measurement run.

5

Preparatory Measurements

To make sure the experimental setup is suited for the PIV- and LIF-measurements that need to be done, some other experiments must be done with the setup first. These experiments include measuring the turbulent statistics of the jet, the vibrations of the camera during movement, and the resulting LIF-calibration to convert image intensity to concentration. This chapter describes how these experiments are done and gives the results of these experiments.

5.1. Turbulent statistics

There has been done quite some research on the characteristics of the velocity profile of the axisymetric turbulent jet, for example by Westerweel et al. [25] and Wygnanski and Fiedler [28]. We want to check whether the velocity profiles from our PIV-measurements match the profiles from the literature.

5.1.1. Experiment

The characteristics of our turbulent jet are found by doing regular PIV-measurements on the beginning of the LIF field of view from the previous chapter without moving the camera for a long time (around 50 seconds, or 500 frames) to accurately determine relevant turbulent statistics in this part of the jet. The considered turbulent statistics are the mean velocity and velocity fluctuations in both directions, as well as the local Reynolds stress.

5.1.2. Results

As mentioned in the previous chapter, the outlet velocity of the nozzle is hard to determine. However, we are able to measure velocities further away from the nozzle and see whether these velocities match what we could expect from the estimated outlet velocity. As mentioned before, the mean velocity U_s in the center of the jet is inversely proportional to the distance from the nozzle, following Equations 5.1 and 5.2.

$$\frac{U_s}{U_0} = \frac{B_u d}{x - x_0} \tag{5.1}$$

which is equivalent to

$$\frac{1}{U_s} = \frac{1}{(B_u d U_0)}(x - x_0) \tag{5.2}$$

Here U_s is the centerline velocity, U_0 is the nozzle outlet velocity, B_u is the decay parameter, assumed to be 5.9, because this equals the closest case from Boersma et al. [4], d is the nozzle diameter and $x - x_0$ is the streamwise distance from the virtual origin. This means that we can compare our mean center velocity in the jet with a theoretical value, considering $Re \approx 5000$. The result of this is shown in Figure 5.1.

The velocity in our measurements is significantly lower than it should be, indicated by a larger slope in Figure 5.1. This could be caused by the fact that the Reynolds number is not as high as calculated, due to an underestimation of the friction in different parts of the system. Another reason could be that we do not measure exactly in the middle of the jet, but slightly next to the center where the mean velocity is lower. Also, the

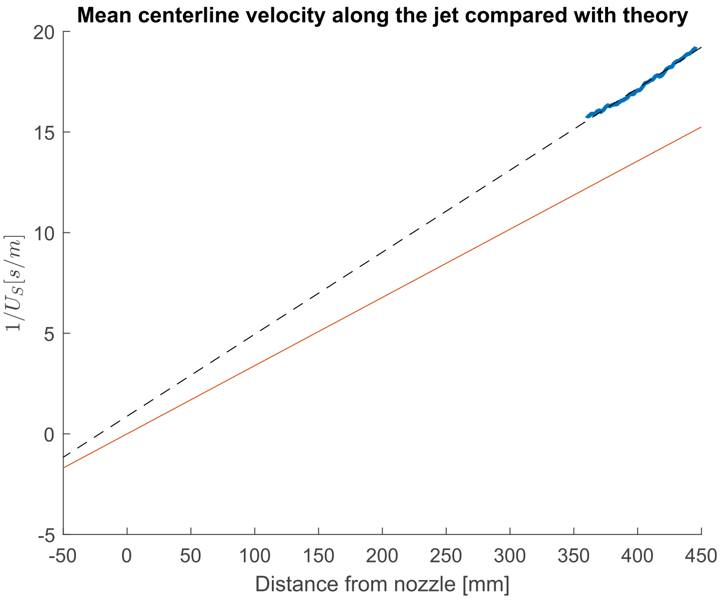

Figure 5.1: Inverse mean velocity in the center of the jet compared with theory. Blue: Measured centerline velocities. Red: Theoretical centerline velocities Black dashed: A linear fit through the measured velocities. The slope of this line gives an indication of the flow properties of the nozzle outlet, and therefore the estimated Reynolds number of out jet. The x-value of the intersection with the y-axis gives information about the virtual origin.

virtual origin seems to be located behind the nozzle, with $x_0 \approx -20mm = -4d$. This decreases the local velocities when compared to the theoretical value. The slope of the black dashed line gives us an estimation of the Reynolds number, since this slope is equal to $1/(B_u dU_0)$, see equation 5.2. From our measurements, assuming $B_u = 5.9$, $(dU_0) = 0.0042m^2/s$, which corresponds to a Reynolds number of 4200, which is significantly lower than designed.

Because the camera is relatively close to the center of the jet, the maximum width of the jet we can consider is approximately $0.9l$ on both sides, so the Turbulent-Non Turbulent interface is not in our field of view. Nevertheless, with this width we can compare the jet characteristics with the literature and therefore it gives us sufficient insight in the turbulent statistics of the jet. First, the mean velocity in streamwise direction could not only be compared with experimental data from literature, but also to the analytical solution from Nieuwstadt et al. [16]:

$$\frac{\bar{u}}{U_s} = \left(1 + \frac{\eta^2}{8B}\right)^{-2} \tag{5.3}$$

with: $\eta = y/l(x)$ and $B = 0.302$. This comparison can be found in Figure 5.2. The comparison of other turbulent statistics, that is streamwiste fluctuations and Reynolds stress, are shown in Figures 5.3 and 5.4 respectively.

From the figures it can be seen that the turbulent statistics of our jet compare well to literature. A few things catch the eye: the mean axial velocity that is also compared to literature seems significantly narrower than the theoretical solution. The explanation for this might be that the factor 0.0965 in the determination of the halfwidth (Equation 3.5) was overestimated. Due to the presence of the wall in our measurements, this factor could be closer to 0.086, following Nieuwstadt et al. and Boersma et al. [4, 16]. This means the macroscale l is smaller, so y/l is bigger and the measured graph becomes less narrow.

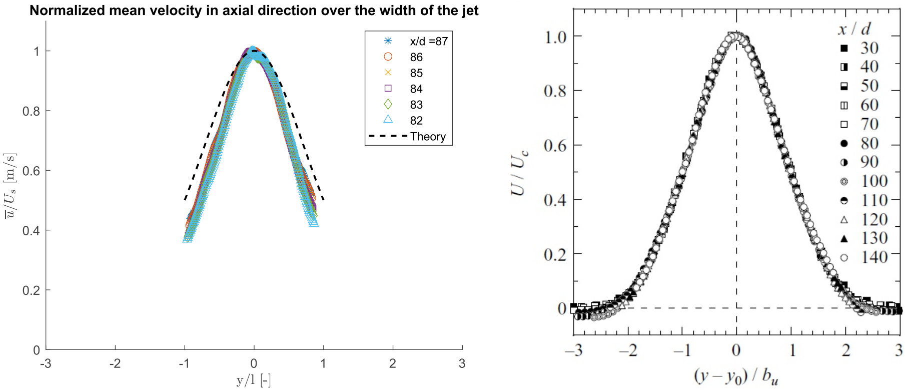

Figure 5.2: Normalized mean velocity across the width jet compared with literature. Left: Normalized mean velocity (measured and theoretical) across the width of the jet from the experiment. Right: Normalized mean velocity across the width of a jet from Westerweel [25]. Note: the b_u in the right graph is the same variable as l in the left graph

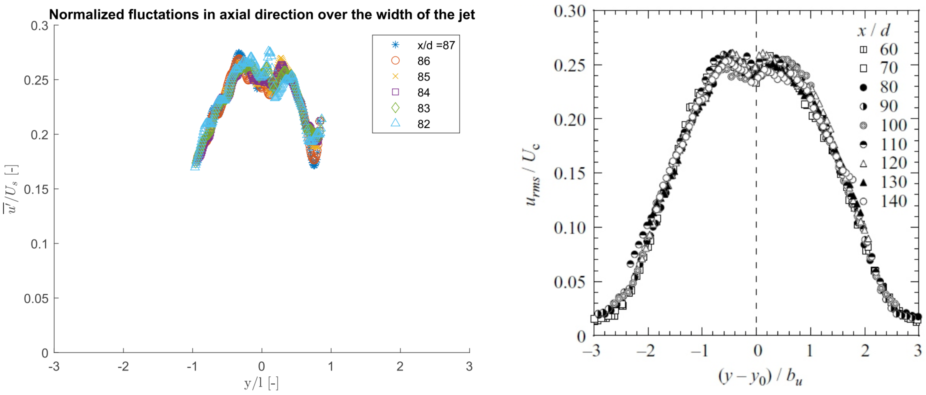

Figure 5.3: Normalized streamwise velocity fluctuations across the jet compared with literature. Left: Normalized streamwise velocity fluctuations across the width of the jet from the experiment. Right: Normalized streamwise velocity fluctuations across the width of a jet from Westerweel [25]. Note: the b_u in the right graph is the same variable as l in the left graph

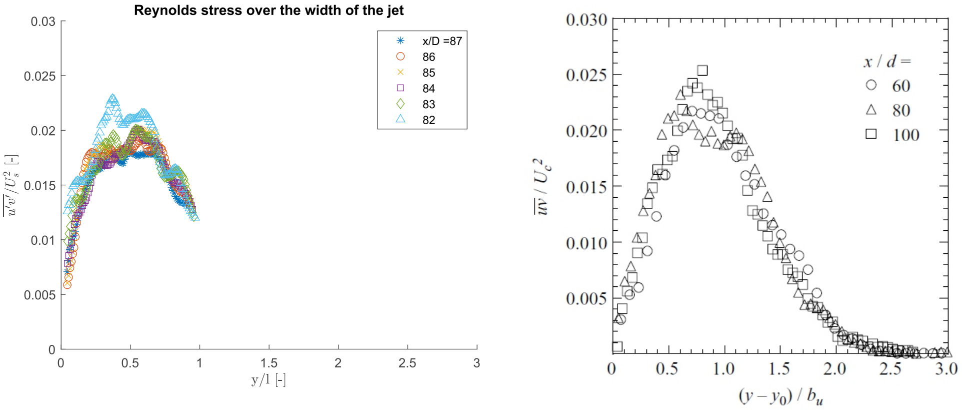

Figure 5.4: Reynolds stress across the jet compared with literature. Left: Normalized Reynolds stress across the width of the jet from the experiment. Right: Reynolds stress across the width of a jet from Westerweel [25]. Note: the b_u in the right graph is the same variable as l in the left graph

5.2. Test of traverse mechanism

The traverse mechanism used in the experimental setup makes use of counting microsteps within the system to obtain a desired velocity or displacement. Because these microsteps are very small, in the order of micrometers, this translation is very precise. However, these microsteps result in a frequent excitation of the mechanical system that includes the cameras and causes this system to vibrate. This has an (yet unknown) effect on the final measurements and therefore this vibration has to be determined.

The vibrations of the camera are measured by doing a quasi-PIV-experiment. Contrary to a normal PIV-experiment, there are no lasers and particles involved, but the camera films multiple sheets of paper with a random particle pattern printed on them to simulate particles. This way, the velocities found by DaVis are only from the movement of the camera, since the paper is stuck to the watertunnel and does not move. The measurements are done with a constant camera velocity of 0.04 and 0.07m/s, which are two candidate velocities for the final measurements. The acceleration of the camera to this velocity is not measured, only the movement with constant velocity. The camera frequency is higher than with the actual measurements (50 Hz instead of 10 Hz), because we can use a smaller field of view and the laser is not a limiting factor. Also the camera is operated in single-frame mode, so per frame only one picture is taken instead of two pictures per time step.

From the measured signal it turns out that there is not only a vibration in the direction of the movement of the camera (horizontal), but also in the vertical direction. The measured signals for both cases in both directions can be found in Figure 5.5.

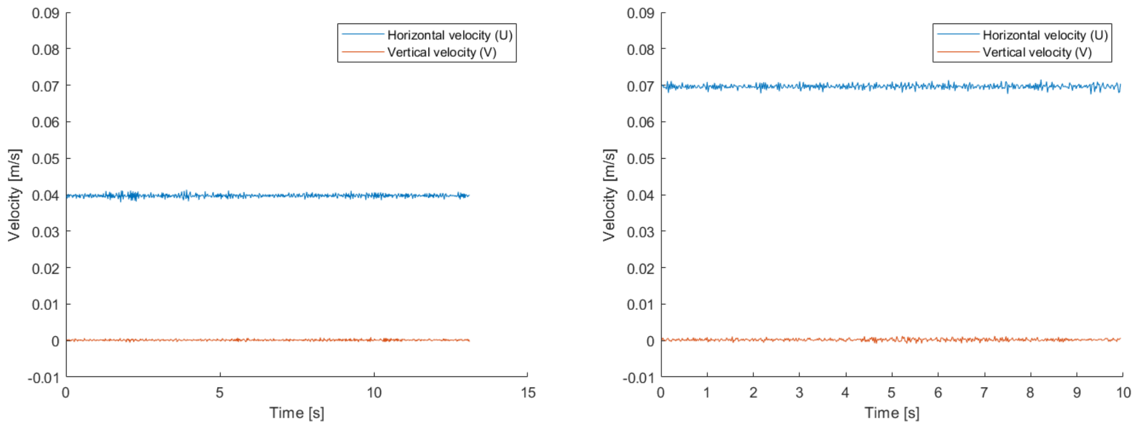

Figure 5.5: Velocity signals of the traverse mechanism Left: 0.04m/s Right: 0.07ms/s

From the signal shown in Figure 5.5 we can clearly see a vibration in the movement. We characterize this vibration by two variables, which are the standard deviation and the extreme values of the vibration. Since this vibration not only has an effect on the measured velocity, but also on the location where we measure the velocity, it is also important to look at the uncertainty of the location of the camera, which can be found by integrating the velocity signal to a distance signal. This distance can be quantified in (milli)metres, but also in number of pixels to see what effect this uncertainty could have on the correlations in DaVis. The results of these calculations can be found in Table 5.1.

Table 5.1: Uncertainties of the traverse speed of the camera. These uncertainties are given in the standard deviation of the velocity, as well the difference between the peak values of the velocity. Using these peak values, we can also estimate the maximum error of the location of the camera, both in [m] as in pixel length

Variable	$U_C = 0.04 m/s$	$U_C = 0.07 m/s$
Standard deviation U $[m/s]$	4.967×10^{-4}	6.681×10^{-4}
Standard deviation V $[m/s]$	2.167×10^{-4}	3.728×10^{-4}
Minimum to maximum U $[m/s]$	0.003402	0.004046
Minimum to maximum V $[m/s]$	0.001501	0.002045
Minimum to maximum distance in X $[m]$	6.804e-05	8.091e-05
Minimum to maximum distance in Y $[m]$	3.001e-05	4.090e-05
Minimum to maximum pixeldistance in X [-]	1.676	1.993
Minimum to maximum pixeldistance in Y [-]	0.7392	1.007

The values from Table 5.1 show that there is a significant standard deviation in the velocity. Therefore the velocity data from the final measurements must be used with caution if absolute velocities are used. In our case, where only velocity gradients play a significant role, a velocity uncertainty that affects the whole image equally is probably negligible. The uncertainty in position could be more troublesome, but since this uncertainty is in the order of 1 or 2 pixels and we are using interrogation windows of 32 pixels, this also will not affect our measurements significantly.

We could consider this vibration as noise over the velocity signal, but this is not appropriate. The vibrations of the cameras are caused by the vibrations of the transverse mechanism, and therefore should be vibrating following the eigenmodes and eigenfrequencies of the structure. These have not been thoroughly investigated, but a first step towards this is looking at a Fast Fourier Transform (FFT) of the velocity signals of Figure 5.5. From a small FFT-analysis and from the values in Table 5.1, it is clear that at $0.07 m/s$ the vibrations are more severe. This could be used as an argument to operate the traverse mechanism at $0.04 m/s$ in the final measurements. Furthermore, the most prominent modes are found around 10 Hz, between 15 Hz and 20 Hz and just below 25 Hz. Measurements in an earlier stage showed there was also a very prominent mode around 50 Hz. If the measured vibrations are unacceptable, these are the modes that need to be damped or suppressed to improve the movement of the traverse mechanism.

5.3. LIF-Calibration

The image intensities in the raw LIF-images do not one-to-one represent concentrations. Because the intensity of the laser sheet is not uniform across the whole measurement area, equal image intensities at different locations do not imply equal concentrations. As long as the concentration is below a certain level, the image intensity at location (x,y) is given by linear function of the concentration. Eisma [6] gave this relation for each individual pixel as follows in Equation 5.4.

$$I(x,y) = \alpha(x,y) I_0(x,y) c^*(x,y) \tag{5.4}$$

Here, the image intensity I at position (x,y) depends on the concentration c^* and the variables $\alpha(x,y)$ and $I_0(x,y)$, which are an efficiency prefactor the local laser intensity respectively. The last two variables are considered as one variable from here on, since the prefactor α can not be found separately and both variables are always needed together in this analysis.

5.3.1. Experiment

In order to find $\alpha(x,y)I_0(x,y)$ for each location in our experiment, a LIF-calibration experiment must be performed. The idea of this experiment is to place a tank with known concentration in the measurement area, see Figure 5.6 and perform LIF-experiments on this tank, by taking images of the tank using the laser and see how the image intensity of the picture varies at different locations. If this is done for different concentrations, a linear graph can be fitted in the (c^*, I)-diagram of each individual pixel, of which the slope is the value $\alpha(x,y)I_0(x,y)$ we were looking for.

The area over which concentration measurements are done is much wider than the field-of-view of the camera, therefore each concentration in the tank is measured at 6 locations, which slightly overlap to make sure that the whole measurement area is covered. In total 7 concentrations are measured. Each individual

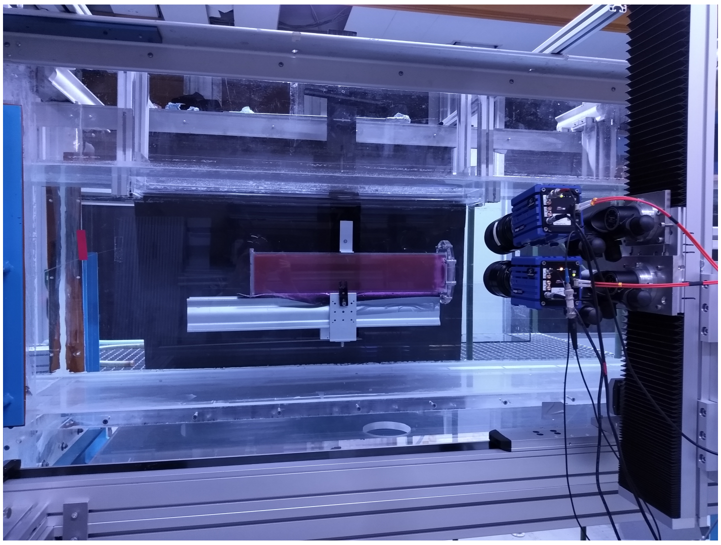

Figure 5.6: LIF-Calibration tank with a known concentration in the setup

measurements contains 100 frames, which are averaged to counteract the effects of the variance in laser intensity.

5.3.2. Processing

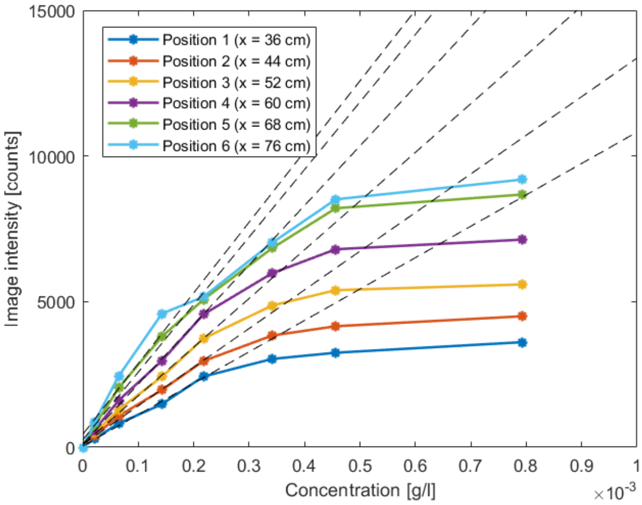

Figure 5.7: Example of a (c^*, I) diagram for the six different locations of the LIF-calibration. The colored lines and point indicate the measured concentrations and their corresponding image intensity. The black lines indicate the fitted linear line through the first 5 points, from which the slope is the needed variable for further analysis

An example of a (c^*, I)-diagram from certain pixels is shown in Figure 5.7. From this diagram, it can be seen that for the three highest concentrations the graph is clearly not linear. This is caused by the fact that at high concentrations there is some attenuation of the light by the Rhodamine. For this reason only the 4 lowest concentrations, together with the origin of the graph, are used to find a linear line that gives $\alpha(x, y)I_0(x, y)$. This is done by fitting a linear least squares fit through these 5 points. When this is done for each pixel, a matrix can be made that shows the value of $\alpha(x, y)I_0(x, y)$ for each location. This matrix is shown in Figure 5.8.

The movement of the camera results in the fact that the pixels of any arbitrary frame do not necessarily coincide with the pixels of the calibration matrix of Figure 5.8. For this reason a third order polynomial is fitted through the values of the calibration matrix, so the value of $\alpha(x, y)I_0(x, y)$ can be found quite easily for

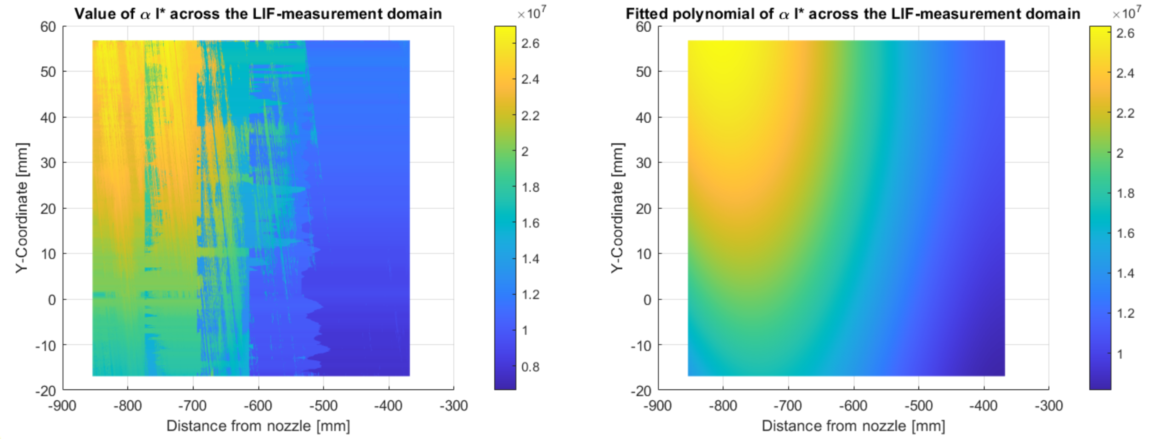

Figure 5.8: Left:Matrix of αI_0 from LIF-Calibration over the LIF-measurement area. Right: Fitted polynomial through the same LIF-calibration matrix. The R^2 value of the fitted polynomial is 0.992

each position by filling in the x- and y-coordinate in the polynomial, see Figure 5.8. The polynomial is given by Equation 5.5 with the coefficients from Table 5.2.

$$\alpha(x,y)I_0(x,y)(x,y) = p_{00} + p_{10}x + p_{01}y + p_{20}x^2 + p_{11}xy + p_{02}y^2 + p_{30}x^3 + p_{21}x^2y + p_{12}xy^2 + p_{03}y^3 \tag{5.5}$$

The concentration from the LIF-images can then be found with the variable from the polynomial using Equation 5.6.

$$c^*(x,y) = \frac{I(x,y)}{\alpha(x,y)I_0(x,y)} \tag{5.6}$$

Table 5.2: Coefficients of the polynomial of equation 5.5, used to transform the image intensity in LIF-measurements into scalar concentration

Coefficient	Value with 95% confidence interval
p_{00}	$4.541 \times 10^7 \pm 0.012 \times 10^7$
p_{10}	$2.433 \times 10^5 \pm 0.006 \times 10^5$
p_{01}	$5.935 \times 10^4 \pm 0.132 \times 10^4$
p_{20}	501.4 ± 1.1
p_{11}	156.0 ± 4.2
p_{02}	764.3 ± 16.7
p_{30}	0.2924 ± 0.0006
p_{21}	0.3586 ± 0.0033
p_{12}	1.776 ± 0.022
p_{03}	-8.06 ± 0.16

6

Results

In this chapter the results of the measurements are shown. First the results of the LIF-measurements are shown in terms of number of zones and the characteristic concentration of each zone. Then the FTLE-field of the same measurements is presented, with a closer look at the integration time and the difference between forward and backward time FTLE. Finally, the FTLE-field and the boundaries of the UCZs are visually compared

6.1. Uniform Concentration Zones

The UCZs are found from the LIF-measurements. As shown in Figure 4.9, each measurement is one scan along the measurement area and consists of 101 LIF-frames and 210 PIV-frames. First, the raw LIF-measurements are calibrated using the calibration polynomial from Chapter 5 and after that a binomial filter with a 5x5 kernel is used to remove noise in the image and smooth the image. After these steps we could use the FCM- and KDE-algorithms from Chapter 2. An example of a concentration field divided into UCZs is shown in Figure 6.1.

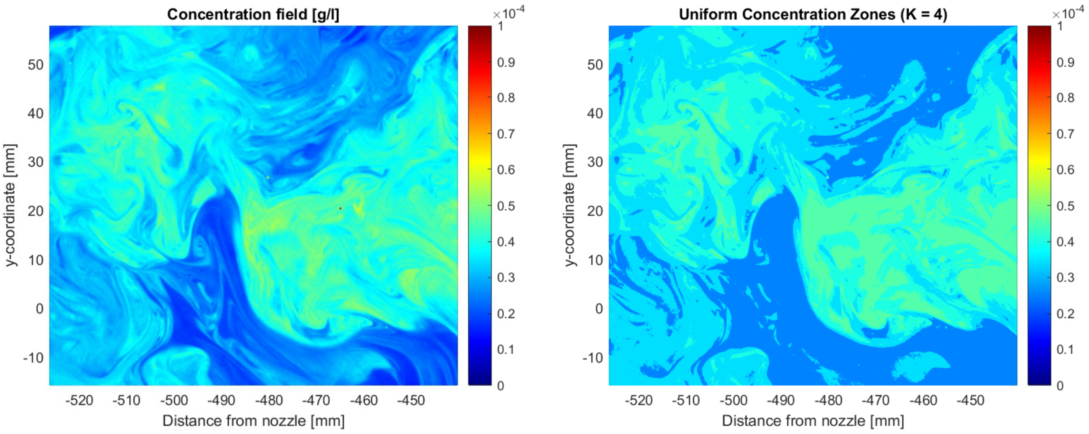

Figure 6.1: An example of Uniform Concentration Zones. Left: A snapshot of a concentration field. Right: The same concentration field divided into 4 Uniform Concentration Zones.

6.1.1. Number of zones

First we look at the number of peaks that the KDE-algorithm finds in the PDF of the concentration fields. This number varies across each snapshot of each measurement; this variation is shown for the first two measurements in Figure 6.2. Here it is shown that the number of peaks varies around 4, and is never higher than 7.

The situation where the number of zones is equal to 2 should be avoided as much as possible, since a concentration field divided in only 2 UCZs does not provide much information about this concentration field and is harder to compare with an FTLE-field. A high number of zones is also not desirable for visual analysis, since then there is not much difference between the concentration field and the UCZs in this concentration field. The number of peaks is only an indication of the number of zones in a snapshot, it is possible that there are observable zones that do not lead to peaks in the PDF. Therefore, it is also defensible to pre-determine the number of zones and use this as input for the FCM-algorithm. For these reasons, visual inspection on the Uniform Concentration Zones will be done on snapshots with 3,4 or 5 zones, which are not pre-determined.

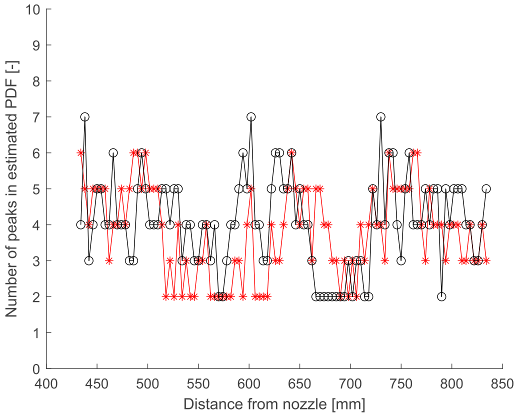

Figure 6.2: The number of peaks found in the PDF estimated by the KDE-algorithm across the first two measurement sets

6.1.2. Distribution of cluster centroids

For comparing purposes, we assumed that the number of UCZs determined by the KDE-algorithm is always equal to 4 in this section, so the number of zones is fixed at 4. This way, we can compare the cluster centroids from the FCM along each snapshot with each other and find a trend in the characteristic concentrations between zones. The values of the found cluster centroids across the first two measurements are shown in Figure 6.3. Here it can be seen that the cluster centroids between these two measurements show a similar downward trend, with approximately the same values. Also, the zones with the highest concentration show a steeper downward gradient than the zones with lower concentrations, so the zones are closer to each other at the end of a measurement set, which is further away from the jet. Both these observations can be explained by the fact that further in the jet more mixing has occurred between earlier zones and the Rhodamine is dispersed over a larger volume in the tunnel, so the average concentration drops and the characteristic concentrations of the UCZs are closer to each other.

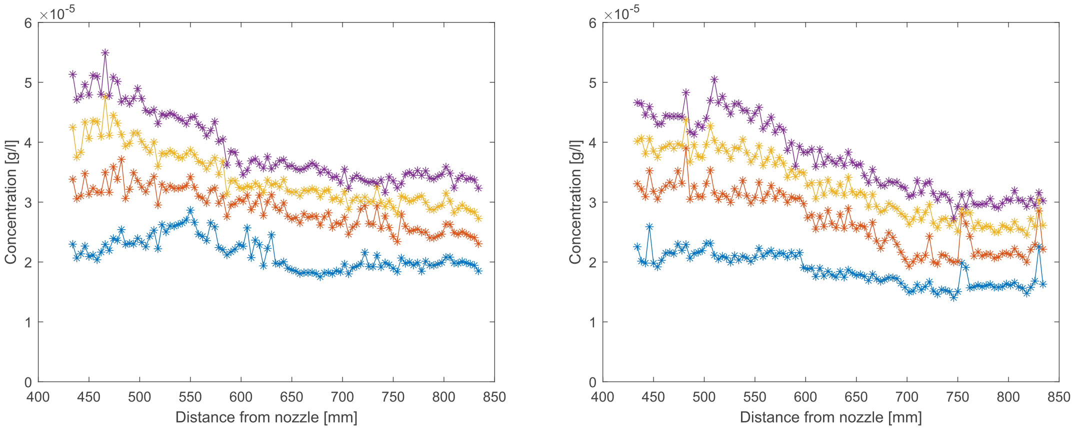

Figure 6.3: Distribution of the cluster centroids from the Fuzzy Cluster Method, with the number of zones fixed at 4, in the first 2 measurements. (Purple: zone 4, yellow: zone 3, red: zone 2, blue: zone 1) Left: Measurement set 1. Right: Measurement set 2.

6.2. FTLE-fields

The FTLE-fields are found by setting the maximum observation time at 4 seconds, or equivalently 40 frames, and interpolating the initial particle matrix with a factor 8, so the number of pixels in both the x- and y-direction will be multiplied with approximately 8, keeping the same minimum and maximum values.

6.2.1. Integration time

As mentioned in the introduction, one of the main goals of this thesis is to build a measurement set in which fluid is observed long enough to obtain sharp ridges in the FTLE-field. Figures 6.4 and 6.5 show the observation times, both forward and backward, for a field-of-view during measurements. This gives us insight in how the FTLE-field is calculated, since it is not possible to keep all particles in the field-of-view for the desired integration time, especially near the borders of the field of view.

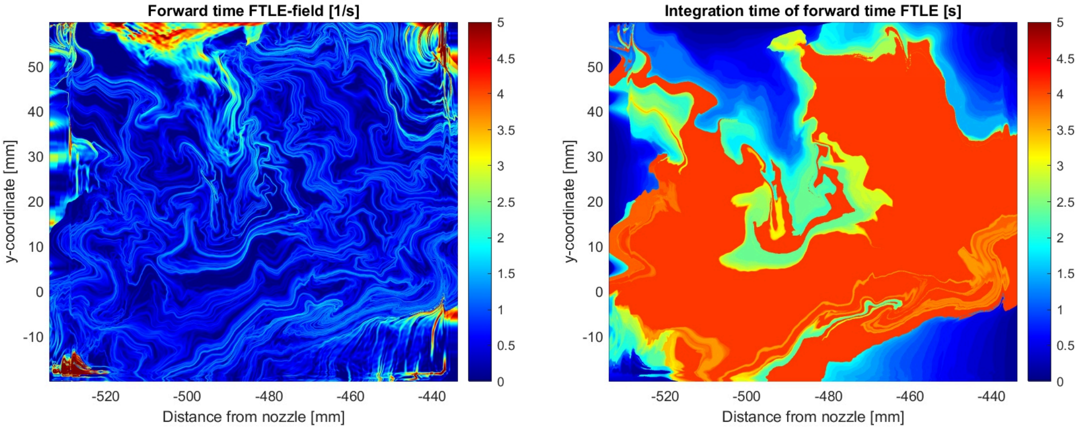

Figure 6.4: Forward time FTLE-field of the same snapshot as Figure 6.1 Left: Forward time FTLE-field. Right: Corresponding integration times used for the calculations of the forward time FTLE-field, with the maximum time set at 4 seconds

Comparing the left and right fields in Figures 6.4 and 6.5 shows an interesting resemblance between a FTLE-field and its integration times. It seems that ridges of the FTLE-field coincide with locations where there is a large gradient in integration time. The fact that a large gradient in integration time leads to high values of the FTLE is a logical result if we consider the definition of the FTLE, that is a measure of fluid separation. A

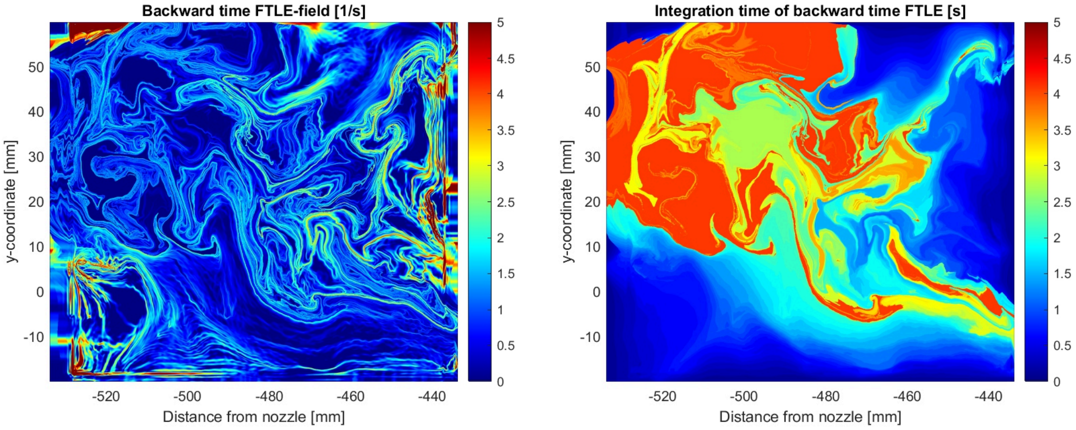

Figure 6.5: Backward time FTLE-field of the same snapshot as Figure 6.1 Left: Backward time FTLE-field. Right: Corresponding integration times used for the calculations of the backward time FTLE-field, with the maximum time set at 4 seconds

large gradient in integration time shows that of two fluid parcels close together, one leaves the field-of-view much earlier than the other one, which is a sign of a high separation rate.

6.2.2. Forward and backward FTLE

There is a significant difference between the forward and backward time FTLE-field, mostly because they represent respectively repelling and attracting LCSs. A first comparison between UCZs and both FTLE-fields is shown in Figures 6.6 and 6.7.

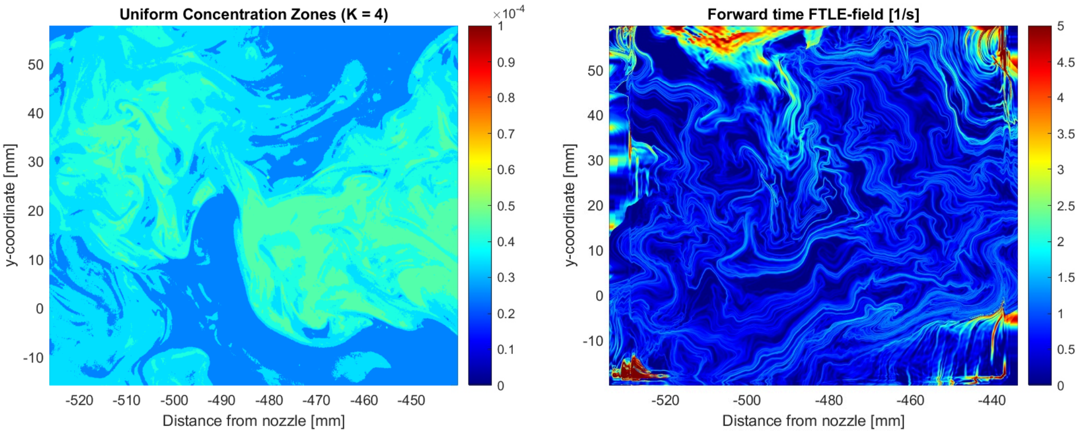

Figure 6.6: Comparison between Uniform Concentration Zones and the forward time FTLE-field. Left: The concentration field divided in Uniform Concentration Zones in the same snapshot as Figure 6.1. Right: Forward time FTLE-field of the same snapshot.

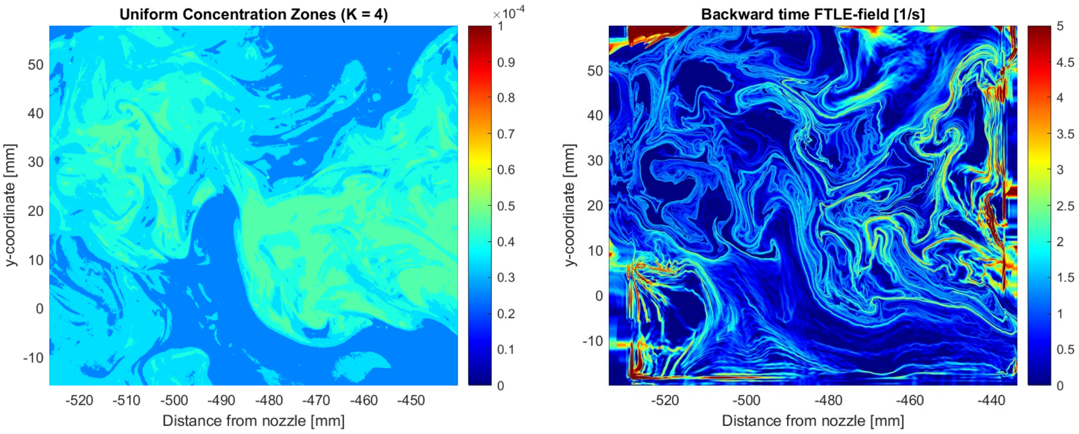

Figure 6.7: Comparison between Uniform Concentration Zones and the backward time FTLE-field. Left: The concentration field divided in Uniform Concentration Zones in the same snapshot as Figure 6.1. Right: Backward time FTLE-field of the same snapshot.

In Figure 6.6 the UCZs are compared to the forward time FTLE-field. The most prominent ridges in this FTLE-field do not seem to have any correlation with the picture that shows the UCZs. The comparison in Figure 6.7 is more promising. Here, some of the more prominent ridges in the backward time FTLE-field seem to be at approximately the same locations as the boundaries of the UCZs. Especially in the top right corner and slightly below the middle the structures look similar. The observation that the backward time FTLE-field shows more resemblance to the UCZs found in the concentration-field than the forward time FTLE-field is clearly seen across the measurement sets, so in a more detailed comparison between UCZs and the FTLE-field in Section 6.3 the emphasis will be on the backward time FTLE.

6.3. Correlation between Uniform Concentration Zones and the FTLE-field

In this section the boundaries of UCZs and the backward time FTLE-field are compared in more detail. First a visual inspection is done by comparing UCZs in the concentration field with the backward time FTLE-field as in Figure 6.7. Then, the boundaries of the UCZs are plotted in the corresponding FTLE-field to take a closer look at their locations and see if they overlap for 2 different snapshots of the measurements.

6.3.1. Visual inspection of the correlation between UCZs and the backward time FTLE.

A first comparison between UCZs and the backward time FTLE-field is shown in Figure 6.7. For a better comparison these two fields are plotted in one picture in Figure 6.8, with the FTLE-field plotted in the same way as Figure 6.7 and the boundaries of the UCZs shown as black contours. Especially the regions in the red circles in Figure 6.8 show clearly that the FTLE is significantly higher near boundaries between UCZs. Figure 6.8 is merely an example: this behaviour also shows at other time instances and other measurement runs, especially at locations where two boundaries of the UCZs are close to each other, so where there is a large concentration gradient perpendicular to the boundaries.

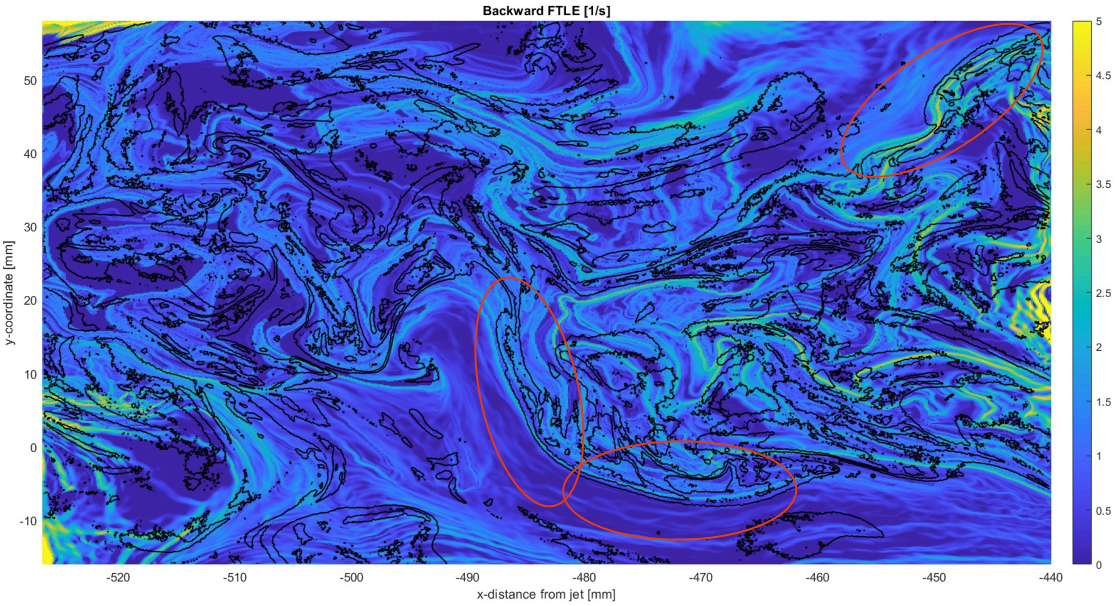

Figure 6.8: For the same snapshot as Figure 6.7: The boundaries of Uniform Concentration Zones (black contours) plotted in the same snapshot as the backward time FTLE-field (background colours). The red circles indicate regions in which there is overlap in the ridges of the FTLE-field and the boundaries of the UCZs, so these are example candidates of regions with a high correlation between UCZ-boundaries and the FTLE-field.

The comparison of Figures 6.7 and 6.8 is done for another snapshot in Figures 6.9 and 6.10, with Figure 6.9 showing the concentration field divided in UCZs, and the backward time FTLE-field separately, and Figure 6.10 showing its respective overlapping picture. More examples can be found in Appendix A. Here the same observations are done as before, that is there is a clear overlap between the boundaries of UCZs and higher regions, or ridges, in the FTLE-field. In these pictures also another observation can be done, that is that in both the concentration field and the FTLE-field mushroom shaped plumes are found at approximately the same locations. The plumes are most prominent in the middle of both fields in Figures 6.9 and 6.10.

In conclusion, the boundaries of Uniform Concentration Zones seem to overlap often with local maxima of the backward time FTLE-field. While comparing this FTLE-field with the concentration field, either divided in UCZs or the raw concentration field, similar structures are observed in both fields, which is probably a sign of significant correlation between the two fields. The forward time FTLE does not seem to correlate with the concentration field.

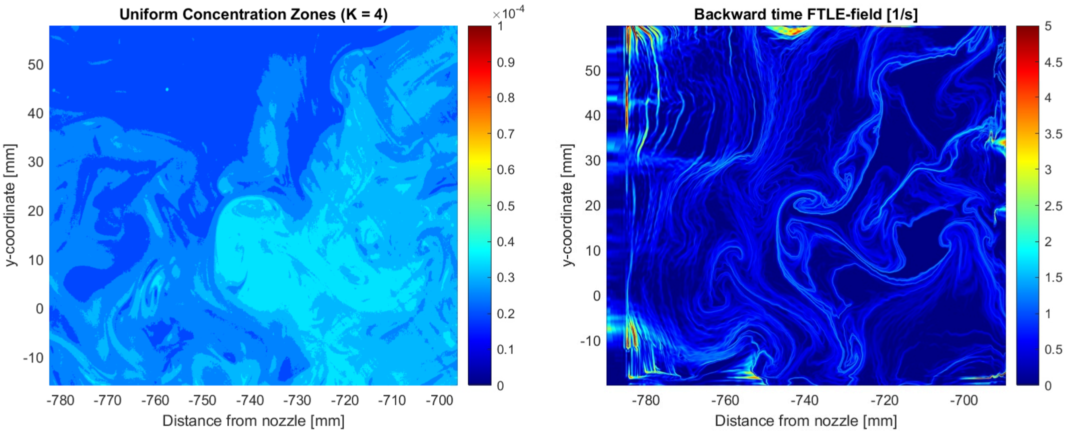

Figure 6.9: Comparison between Uniform Concentration Zones and the backward time FTLE-field in measurement 1, frame 85. Left: The concentration field divided in Uniform Concentration Zones. Right: Backward time FTLE-field of the same snapshot.

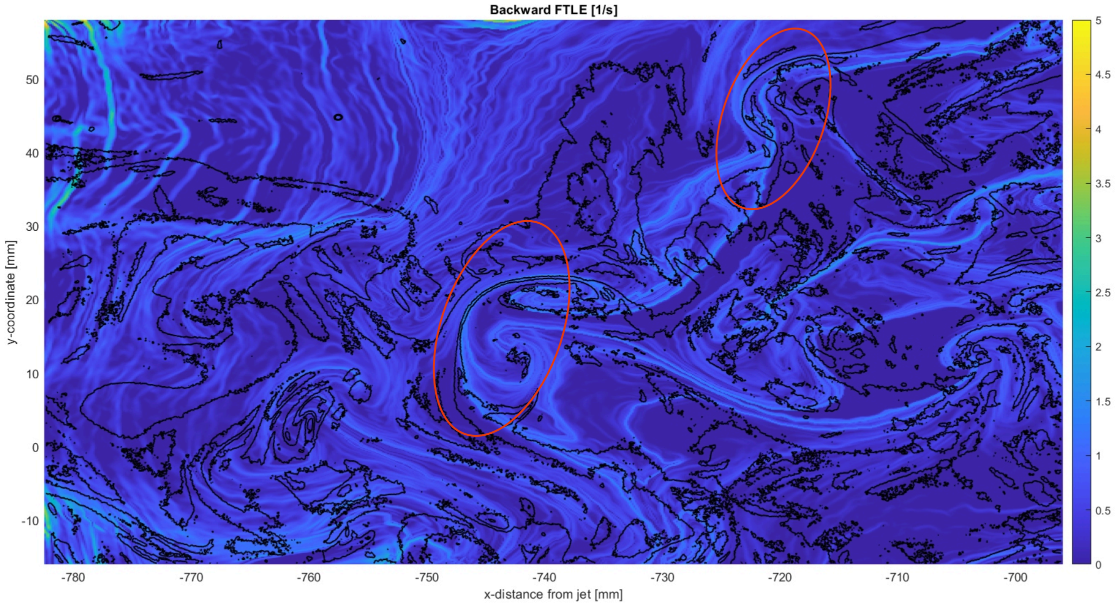

Figure 6.10: For the same snapshot as Figure 6.9: The boundaries of Uniform Concentration Zones (black contours) plotted in the same snapshot as the backward time FTLE-field (background colours). The red circles indicate regions in which there is overlap in the ridges of the FTLE-field and the boundaries of the UCZs, so these are example candidates of regions with a high correlation between UCZ-boundaries and the FTLE-field.

7

Conclusions and recommendations

7.1. Conclusion

In this thesis, experiments on a turbulent jet with simultaneous PIV- and LIF-measurements are performed in the Aero- and Hydrodynamics Lab at the 3ME-faculty of the TU Delft. These experiments are designed to be able to find Uniform Concentration Zones in the concentration field and a distinct Finite Time Lyapunov Exponent-field using the velocity field. For this reason, two cameras are installed on a traverse mechanism in order to move the cameras parallel to the flow. This way turbulent structures remain longer in the field-of-view of the cameras. Using this setup two measurement sets, containing velocity and concentration measurements via PIV and LIF respectively, were recorded. The first set contains 26 measurements at $Re = 5000$, the second set contains 10 measurements at $Re = 10000$. Using the data in these sets, Uniform Concentration Zones and the Finite Time Lyapunov Exponent, both forward and backward in time, were found successfully.

It was found by visually comparing the FTLE-field and the Uniform Concentration Zones that the forward time FTLE showed no correlation with the boundaries of Uniform Concentration Zones. However, the backward time FTLE showed similar structures as the concentration field and visible ridges in this FTLE-field seem to overlap with the boundaries of UCZs, especially in regions where the UCZs display large gradients.

7.2. Recommendations

Although the results of the measurements in terms of the correlation between UCZs and the FTLE-field are quite promising, the experiment itself could be improved in some ways. First, the laser sheet was built up using mirrors that were placed above the far end of the measurement zone, which resulted in a laser intensity profile across the measurement area that had its peak almost at the end of this measurement area. This is not necessarily a problem for concentration measurements, because the LIF-calibration takes this profile into account, but placing the final mirror directly above the middle of the measurement area leads to higher intensity in the middle of the measurement area, which enables the use of a larger part of the dynamical range of the cameras. Also, lining up the laser sheet along the center of the jet will be easier in this case.

The use of the double-pulsed Nd-Yag PIV-laser resulted in some issues regarding the LIF-measurements. This kind of laser has some variance in intensity between pulses, which results in a variance in concentration measurements, since measured concentration is proportional to laser intensity. We tried to measure this variance in laser intensity using a photo-diode, but these measurements were insufficient. What we did discover using this photo-diode is that when our laser was triggered externally with a non-constant frequency, the laser intensity showed a trend in intensity that is far from ideal. Performing reliable concentration measurements with a similar laser requires a constant triggering frequency and a better way to measure the variance in laser intensity, or a different laser should be used.

Also, the way the jet is made inside the water tunnel could be improved. The overflowing barrel principle works fine and gives a constant outlet velocity, but this velocity is hard to precisely control due to not fully known friction values and increasing the height of the tube from the barrel to the reservoir was not very accurate. A pump that controls the flow directly would be recommended if more precision is needed in calculating the Reynolds number. Finally the amount of Rhodamine inside the barrel and reservoir was hard to control, so this resulted in some variance in concentration between measurements. Especially at the last sets where there was some buildup of Rhodamine in the water tunnel, which skewed the concentration measurements a bit. In this thesis we were interested in instantaneous snapshots of the concentration and we did not necessarily compare snapshots with each other. Therefore, the issues with the Rhodamine and the variance in laser intensity did not affect the main results and conclusions found in this thesis. However, for other purposes these concentration measurements should be used with caution.

The found results of correlation between Uniform Concentration Zones and the FTLE-field are based purely on visual inspection. Further research is recommended in statistically compare both the FTLE-fields with Uniform Concentration Zones, for example via conditional averaging. This way, the visually found correlation between the boundaries of UCZs and the backward time FTLE-field can be validated, as well as the lack of correlation between the forward time FTLE-field and the UCZ-boundaries.

A

More results

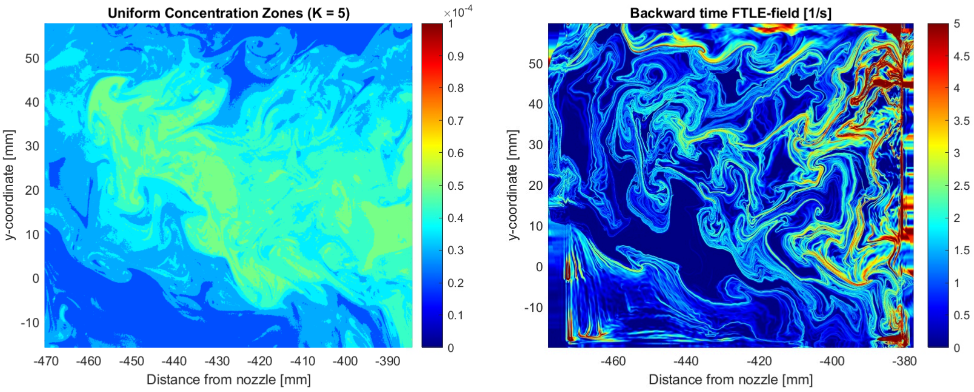

Figure A.1: Comparison between Uniform Concentration Zones and the backward time FTLE-field in measurement 1, frame 7. Left: The concentration field divided in Uniform Concentration Zones. Right: Backward time FTLE-field of the same snapshot.

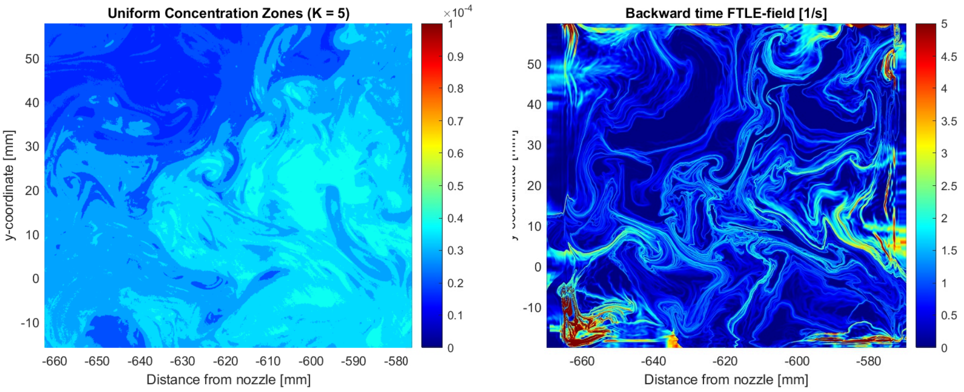

Figure A.2: Comparison between Uniform Concentration Zones and the backward time FTLE-field in measurement 2, frame 55. Left: The concentration field divided in Uniform Concentration Zones. Right: Backward time FTLE-field of the same snapshot.

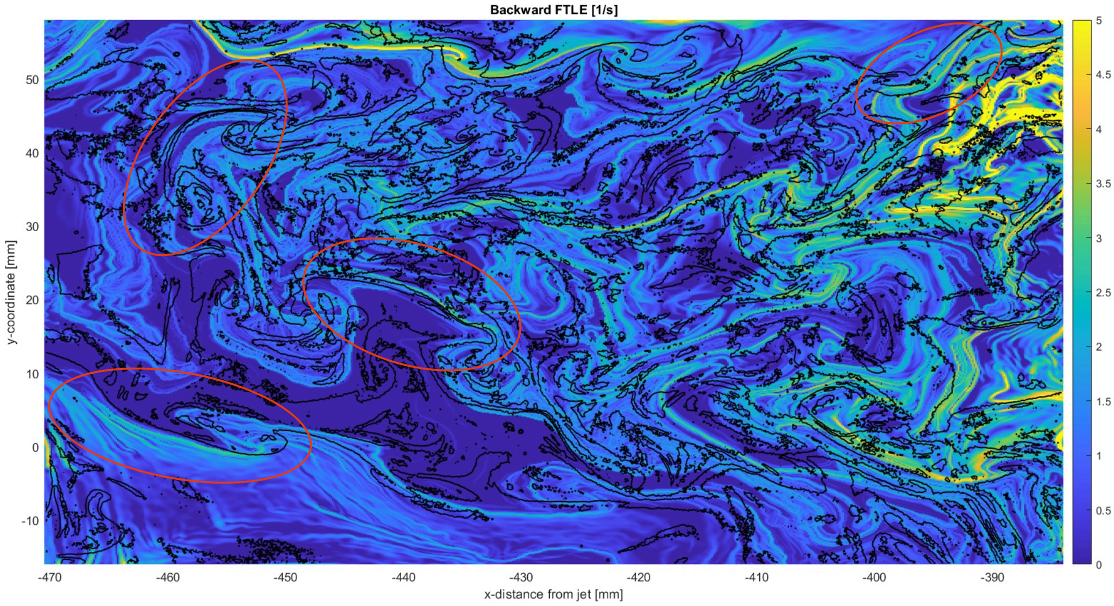

Figure A.3: For the same snapshot as Figure A.1: The boundaries of Uniform Concentration Zones (black contours) plotted in the same snapshot as the backward time FTLE-field (background colours). The red circles indicate regions in which there is overlap in the ridges of the FTLE-field and the boundaries of the UCZs, so these are example candidates of regions with a high correlation between UCZ-boundaries and the FTLE-field.

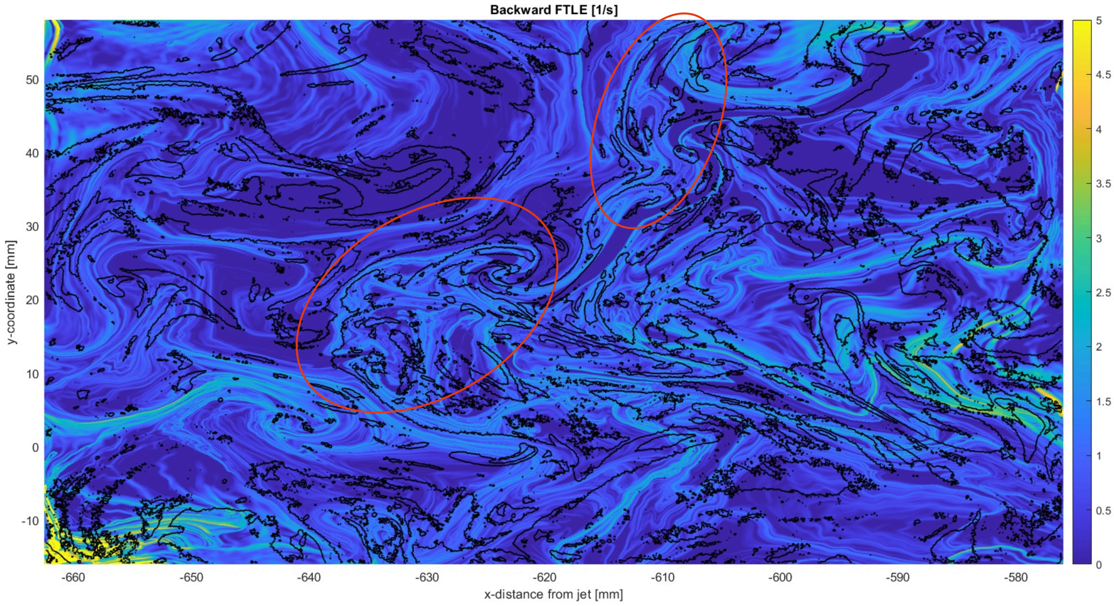

Figure A.4: For the same snapshot as Figure A.2: The boundaries of Uniform Concentration Zones (black contours) plotted in the same snapshot as the backward time FTLE-field (background colours). The red circles indicate regions in which there is overlap in the ridges of the FTLE-field and the boundaries of the UCZs, so these are example candidates of regions with a high correlation between UCZ-boundaries and the FTLE-field.

Bibliography

[1] R. J. Adrian. *Particle image velocimetry*. Cambridge Aerospace series. Cambridge University Press, New York, 2011. ISBN 9780521440080 (hardback) 0521440084 (hardback).

[2] M. R. Allshouse and T. Peacock. Refining finite-time lyapunov exponent ridges and the challenges of classifying them. *Chaos*, 25(8), 2015. ISSN 1054-1500. doi: Artn08741010.1063/1.4928210. URL `<GotoISI>://WOS:000360657900030https://aip.scitation.org/doi/pdf/10.1063/1.4928210`.

[3] J. C. Bezdek. A convergence theorem for the fuzzy isodata clustering algorithms. *IEEE Trans Pattern Anal Mach Intell*, 2(1):1–8, 1980. ISSN 0162-8828 (Print) 0098-5589 (Linking). doi: 10.1109/tpami.1980.4766964. URL `https://www.ncbi.nlm.nih.gov/pubmed/22499617`.

[4] B. J. Boersma, G. Brethouwer, and F. T. M. Nieuwstadt. A numerical investigation on the effect of the inflow conditions on the self-similar region of a round jet. *Physics of Fluids*, 10(4):899–909, 1998. ISSN 1070-6631. doi: Doi10.1063/1.869626. URL `<GotoISI>://WOS:000072757300015https://aip.scitation.org/doi/pdf/10.1063/1.869626`.

[5] S. L. Brunton and C. W. Rowley. Fast computation of finite-time lyapunov exponent fields for unsteady flows. *Chaos*, 20(1), 2010. ISSN 1054-1500. doi: Artn01750310.1063/1.3270044. URL `<GotoISI>://WOS:000276211400038https://aip.scitation.org/doi/pdf/10.1063/1.3270044`.

[6] J. Eisma. *Pollutant dispersion in wall-bounded turbulent flows*. Phd thesis, 2016.

[7] J. Eisma, J. Westerweel, G. Ooms, and G. E. Elsinga. Interfaces and internal layers in a turbulent boundary layer. *Physics of Fluids*, 27(5), 2015. ISSN 1070-6631. doi: Artn05510310.1063/1.4919909. URL `<GotoISI>://WOS:000355922800037https://aip.scitation.org/doi/pdf/10.1063/1.4919909`.

[8] D. S. Fan, J. L. Xu, M. X. Yao, and J. P. Hickey. On the detection of internal interfacial layers in turbulent flows. *Journal of Fluid Mechanics*, 872:198–217, 2019. ISSN 0022-1120. doi: 10.1017/jfm.2019.343. URL `<GotoISI>://WOS:000470731800001https://www.cambridge.org/core/services/aop-cambridge-core/content/view/1600E66E62C06B467249C2A8E53B7E2E/S0022112019003434a.pdf/div-class-title-on-the-detection-of-internal-interfacial-layers-in-turbulent-flows-div.pdf`.

[9] M. Farazmand and G. Haller. Computing lagrangian coherent structures from their variational theory. *Chaos*, 22(1), 2012. ISSN 1054-1500. doi: Artn01312810.1063/1.3690153. URL `<GotoISI>://WOS:000302576900028https://aip.scitation.org/doi/pdf/10.1063/1.3690153`.

[10] A. Hadjighasem, M. Farazmand, D. Blazevski, G. Froyland, and G. Haller. A critical comparison of lagrangian methods for coherent structure detection. *Chaos*, 27(5), 2017. ISSN 1054-1500. doi: Artn05310410.1063/1.4982720. URL `<GotoISI>://WOS:000402804200006https://aip.scitation.org/doi/10.1063/1.4982720`.

[11] G. Haller. Lagrangian coherent structures. *Annual Review of Fluid Mechanics, Vol 47*, 47:137–162, 2015. ISSN 0066-4189. doi: 10.1146/annurev-fluid-010313-141322. URL `<GotoISI>://WOS:000348560400007https://www.annualreviews.org/doi/pdf/10.1146/annurev-fluid-010313-141322`.

[12] G. Haller and F. J. Beron-Vera. Geodesic theory of transport barriers in two-dimensional flows. *Physica D-Nonlinear Phenomena*, 241(20):1680–1702, 2012. ISSN 0167-2789. doi: 10.1016/j.physd.2012.06.012. URL `<GotoISI>://WOS:000309641200002`.

[13] K. T. Kiger and C. Pan. Piv technique for the simultaneous measurement of dilute two-phase flows. *Journal of Fluids Engineering-Transactions of the Asme*, 122(4):811–818, 2000. ISSN 0098-2202. doi: Doi10.1115/1.1314864. URL <GotoISI>://WOS:000167106200026https://watermark.silverchair.com/811_1.pdf?token=AQECAHi208BE49Ooan9kkhW_Ercy7Dm3ZL_
9Cf3qfKAc485ysgAAA5MwggOPBgkqhkiG9w0BBwagggOAMIIDfAIBADCCA3UGCSqGSIb3DQEHATAeBglghkgBZQMEAS4w
Bd7sObS2yIem02teNolbrOL7XKIU7uv6PwvO33fWPzrq3xzfpGHz1g9U_ElAOWvK7CqcUbHTJ1W9jXtS1E8jCOuzV_
4C9Z-YzALiAbH6PjuvTbgkhS1T3YI61a7e_f2qG1M6OrlvB9eQT4_ttv3cLEaA2lvKzsqevibCDo8SIqPvojuiV1OtdMV
AtJURX1ZOeeOY-y2kNMQRY5R-odSJJGuEIA3cg_Ym9tFIVtf-RS7ae4Y-kRkpVTGkJjLdd1ghhcDAfqy4-O_
skLVJG4INvoK2cDtW9kaSFF_JN9tupHX8mfE9x4-7apZHhCxljNlNtcM5VxpYKiKEg5_
ChB5OKX0jLkR8PGHO1wmlOjbQcbB2dRGvPsBxgafdruV5dTRcaYN5DfSEl0y-elKFhjwfHpSGfmbg2D7QC4ciWZDnAqxw
CE-5q9yNcEinvpMdjqCEqVcdTqpZFqK5QrzmvnAfQv2uZ7KoyTmc3QxCXrkwA0aO8uNye6YCJJ1jsJsypYRp7-YDefZMg
mUqMfiTYzCoiDlTWVWah1eahci6YiZoMAXI4_wfilSQzJTEjjb9jE_OtwETmvIW4Ep8oFuDBrk8kY8QABv3m--_
ZGeEMpVIwq9YN_jMRnz10BaUxwJ9_cY2327ndCWsP5LdsMsiPNXBiAJ7fkcjEo04yIyydJvhmp0i1-LF_
c2bUYM4P372l7fkptstYlKpCIT7HqXDEdAOFMwWL0pWpufwDW1yLE6JCKkzLedn5E3FSHG9NlVwT4aU87iH_
2YhhBjr5jSMVIHsBWHTx5JrLLbDFGLM_7QBspLiTY0.

[14] M. Mathur, G. Haller, T. Peacock, J. E. Ruppert-Felsot, and H. L. Swinney. Uncovering the lagrangian skeleton of turbulence. *Phys Rev Lett*, 98(14):144502, 2007. ISSN 0031-9007 (Print) 0031-9007 (Linking). doi: 10.1103/PhysRevLett.98.144502. URL https://www.ncbi.nlm.nih.gov/pubmed/17501277.

[15] C. D. Meinhart and R. J. Adrian. On the existence of uniform momentum zones in a turbulent boundary-layer. *Physics of Fluids*, 7(4):694–696, 1995. ISSN 1070-6631. doi: Doi10.1063/1.868594. URL <GotoISI>://WOS:A1995QP77800004.

[16] F. T. M. Nieuwstadt, Bendiks J. Boersma, Jerry Westerweel, and Just Wolf. *Turbulence Introduction to Theory and Applications of Turbulent Flows*. ISBN 978-3-319-31599-7. URL http://sfx.ethz.ch/sfx_locater?sid=ALEPH:EBI01&genre=book&isbn=9783319315997.

[17] J. F. Peng and J. O. Dabiri. The 'upstream wake' of swimming and flying animals and its correlation with propulsive efficiency. *Journal of Experimental Biology*, 211(16):2669–2677, 2008. ISSN 0022-0949. doi: 10.1242/jeb.015883. URL <GotoISI>://WOS:000258297000017https://jeb.biologists.org/content/jexbio/211/16/2669.full.pdf.

[18] A. Pentek, T. Tel, and Z. Toroczkai. Chaotic advection in the velocity-field of leapfrogging vortex pairs. *Journal of Physics a-Mathematical and General*, 28(8):2191–2216, 1995. ISSN 0305-4470. doi: Doi10.1088/0305-4470/28/8/013. URL <GotoISI>://WOS:A1995QV90400013https://iopscience.iop.org/article/10.1088/0305-4470/28/8/013.

[19] S. G. Raben, S. D. Ross, and P. P. Vlachos. Computation of finite-time lyapunov exponents from time-resolved particle image velocimetry data. *Experiments in Fluids*, 55(1), 2014. ISSN 0723-4864. doi: ARTN163810.1007/s00348-013-1638-8. URL <GotoISI>://WOS:000332151400009.

[20] S. C. Shadden, F. Lekien, and J. E. Marsden. Definition and properties of lagrangian coherent structures from finite-time lyapunov exponents in two-dimensional aperiodic flows. *Physica D-Nonlinear Phenomena*, 212(3-4):271–304, 2005. ISSN 0167-2789. doi: 10.1016/j.physd.2005.10.007. URL <GotoISI>://WOS:000234005900008.

[21] B. W. Silverman. *Density estimation for statistics and data analysis*. Monographs on statistics and applied probability. Chapman and Hall, London ; New York, 1986. ISBN 0412246201. URL Publisherdescriptionhttp://www.loc.gov/catdir/enhancements/fy0738/85021347-d.html.

[22] P. D. Swanson and J. M. Ottino. A comparative computational and experimental-study of chaotic mixing of viscous fluids. *Journal of Fluid Mechanics*, 213:227–249, 1990. ISSN 0022-1120. doi: Doi10.1017/S0022112090002300. URL <GotoISI>://WOS:A1990DC04000014https://www.cambridge.org/core/services/aop-cambridge-core/content/view/E4D73EAE9EA37131926063D87C5CBDC1/S0022112090002300a.pdf/
div-class-title-a-comparative-computational-and-experimental-study-of-chaotic-mixing-of-visc
pdf.

[23] M. J. Twardos, P. E. Arratia, M. K. Rivera, G. A. Voth, J. P. Gollub, and R. E. Ecke. Stretching fields and mixing near the transition to nonperiodic two-dimensional flow. *Physical Review E*, 77 (5), 2008. ISSN 1539-3755. doi: ARTN05631510.1103/PhysRevE.77.056315. URL `<GotoISI>://WOS:000256885500052https://journals.aps.org/pre/pdf/10.1103/PhysRevE.77.056315`.

[24] G. A. Voth, G. Haller, and J. P. Gollub. Experimental measurements of stretching fields in fluid mixing. *Phys Rev Lett*, 88(25 Pt 1):254501, 2002. ISSN 0031-9007 (Print) 0031-9007 (Linking). doi: 10.1103/PhysRevLett.88.254501. URL `https://www.ncbi.nlm.nih.gov/pubmed/12097088`.

[25] J. Westerweel, C. Fukushima, J. M. Pedersen, and J. C. R. Hunt. Momentum and scalar transport at the turbulent/non-turbulent interface of a jet. *Journal of Fluid Mechanics*, 631:199–230, 2009. ISSN 0022-1120 1469-7645. doi: 10.1017/s0022112009006600.

[26] Frank M. White. *Fluid mechanics*. McGraw Hill, New York, N.Y., 7th edition, 2011. ISBN 00240361061.

[27] Z. D. Wilson, M. Tutkun, and R. B. Cal. Identification of lagrangian coherent structures in a turbulent boundary layer. *Journal of Fluid Mechanics*, 728:396–416, 2013. ISSN 0022-1120. doi: 10.1017/jfm.2013.214. URL `<GotoISI>://WOS:000321835100021`.

[28] I. Wygnanski and H. Fiedler. Some measurements in the self-preserving jet. *Journal of Fluid Mechanics*, 38(3):577–612, 2006. ISSN 0022-1120 1469-7645. doi: 10.1017/s0022112069000358.